Cell Systems

Article

Live-cell single-vRNP imaging identifies viral gene expression signatures that shape influenza infection heterogeneity

Graphical abstract

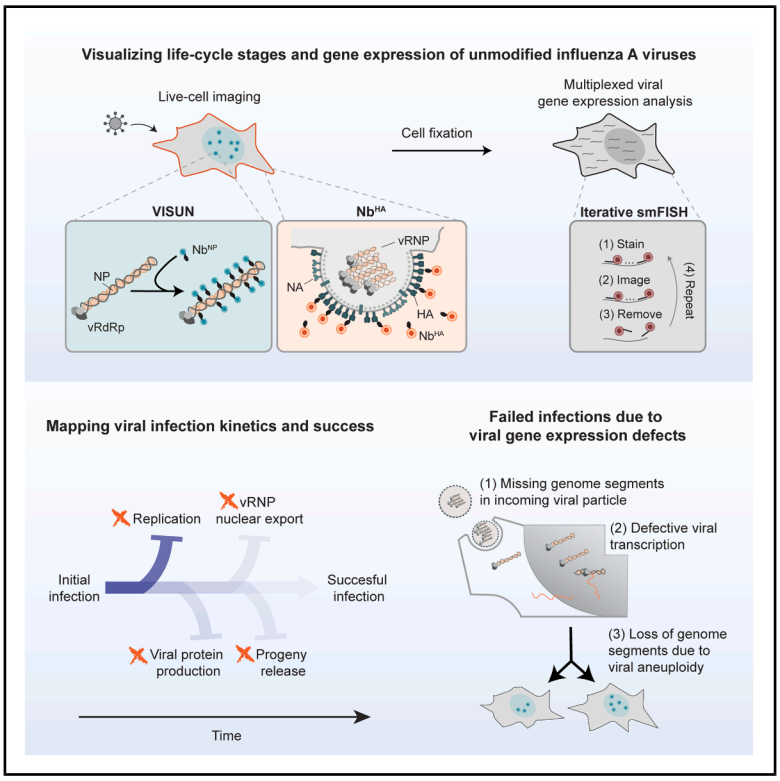

Highlights

- Live-cell tracking of the influenza A virus life cycle through single-vRNP imaging
- More than 95% of IAV infections fail to produce viral progeny
- Many IAV infections are unsuccessful due to transcriptionally inactive vRNPs
- Naturally occurring single-gene KOs show that vRNP nuclear export does not require HA

Authors

Huib H. Rabouw, Janin Schokolowski, Micha Müller, ..., Hans Clevers, Ron A.M. Fouchier, Marvin E. Tanenbaum

Correspondence

m.tanenbaum@hubrecht.eu

In brief

In this study, an imaging technology, "VISUN," is developed that allows live-cell visualization of unmodified influenza virus during infection with single-vRNP resolution. Combining VISUN with multiplex gene expression analysis revealed the origins of viral infection heterogeneity and identified important functions of viral proteins.

Rabouw et al., 2026, Cell Systems *17*, 101489
February 18, 2026
https://doi.org/10.1016/j.cels.2025.101489

CellPress

Cell Systems

CellPress
OPEN ACCESS

Article

Live-cell single-vRNP imaging identifies viral gene expression signatures that shape influenza infection heterogeneity

Huib H. Rabouw,[1,5] Janin Schokolowski,[1,5] Micha Müller,[1,5] Matthijs J.D. Baars,[1] Antonella F.M. Dost,[1] Theo M. Bestebroer,[2] Jakob Püschel,[1] Hans Clevers,[1,3] Ron A.M. Fouchier,[2] and Marvin E. Tanenbaum[1,4,6,*]

[1]Hubrecht Institute-KNAW, Oncode Institute, and University Medical Center Utrecht, 3584 CT Utrecht, the Netherlands
[2]Department of Viroscience, Erasmus University Medical Center, 3015 GD Rotterdam, the Netherlands
[3]Institute of Human Biology (IHB), Roche Pharma Research and Early Development, Roche Innovation Center, 4070 Basel, Switzerland
[4]Department of Bionanoscience, Kavli Institute of Nanoscience Delft, Delft University of Technology; 2628 CJ Delft, the Netherlands
[5]These authors contributed equally
[6]Lead contact
*Correspondence: m.tanenbaum@hubrecht.eu
https://doi.org/10.1016/j.cels.2025.101489

SUMMARY

Cell-to-cell heterogeneity in infection outcome is a general feature of most viruses, but the underlying mechanisms are poorly understood. Here, we developed a live-cell single-molecule imaging technology to visualize infection by unmodified influenza A viruses (IAVs) with unprecedented resolution. Using this approach, we generated a detailed kinetic map of IAV infection, which identified viral ribonucleoprotein (vRNP) replication, nuclear export, and virion budding as important sources of heterogeneity. Mechanistically, we show that infection heterogeneity is caused by differential viral gene expression signatures, resulting from widespread transcriptional defects and loss of viral genome segments. For example, loss of NS, but surprisingly not polymerase subunits, severely delays replication onset, and loss of M and NS, but not HA, underlies vRNP nuclear export defects. In summary, our work identifies the origin and consequences of infection heterogeneity and provides a broadly applicable technology that allows high-resolution phenotyping of unmodified IAVs and other negative-strand RNA viruses.

INTRODUCTION

Influenza A virus (IAV) causes a major health and economic burden on society through annual seasonal outbreaks and occasional pandemics.[1–3] The negative-strand RNA genome of IAV has a total length of ~15 kb, distributed over eight viral genomic RNAs (vRNAs), called genome segments, each of which contains one or more open reading frames that encode viral proteins. Each genome segment is encapsidated by the nucleoprotein (NP) and bound by one copy of the viral RNA-dependent RNA polymerase (vRdRp), consisting of the polymerase basic protein 1 (PB1), polymerase basic protein 2 (PB2), and polymerase acidic protein (PA),[4] to form a stable unit called the viral ribonucleoprotein (vRNP).[5]

Upon attachment to the host cell plasma membrane, IAV virions undergo endocytosis, and vRNPs are subsequently released into the cytoplasm, after which they translocate to the nucleus, where they reside for the majority of the infection cycle. In the nucleus, vRNPs undergo transcription to produce polyadenylated and capped viral mRNAs, which are translated by host ribosomes. At some point in the IAV infection cycle, vRNPs are thought to switch from transcription to replication through mechanisms that are incompletely understood.[6–10] Once sufficient viral proteins and vRNPs have been synthesized, nuclear export of the vRNPs is triggered, and vRNPs are trafficked to the plasma membrane, where assembly of progeny virions takes place.

Although the canonical IAV infection cycle is relatively well understood, infections by IAV, like many viruses, can be highly heterogeneous at the single-cell level in terms of kinetics, success, and host cell responses.[11–15] Heterogeneity in events that occur during early infection may be especially relevant, as small (kinetic) differences in early infection could become amplified to cause major differences in infection outcome. Despite its importance, infection heterogeneity is poorly understood, largely due to limitations of current methodology. Many techniques to study virus infection make use of bulk cell analyses, which only provide cell population averages, masking single-cell heterogeneity. Most techniques that gather single-cell information require cell fixation or lysis and thus only provide snapshot information, making it challenging to link early infection heterogeneity to late-stage infection outcomes. Events during very early infection have been especially challenging to study, because the levels of viral protein and RNA present during early infection are

Please cite this article in press as: Rabouw et al., Live-cell single-vRNP imaging identifies viral gene expression signatures that shape influenza infection heterogeneity, Cell Systems (2025), https://doi.org/10.1016/j.cels.2025.101489

typically below the detection sensitivity threshold, resulting in a major gap in knowledge on IAV infection. To tackle these limitations, we have recently developed *virus infection real-time imaging* (*VIRIM*), a method to visualize infection by positive-strand RNA viruses with single-vRNA resolution.[16] Although VIRIM provided initial insights into early infection dynamics and heterogeneity, the requirement for vRNA translation for visualization limits its use to positive-strand RNA viruses only and hampers observation of many key steps in the viral infection cycle, including viral entry, replication, and virion budding. Moreover, defective vRNAs are not observed, limiting the understanding of infection heterogeneity and success. Finally, VIRIM requires genetic engineering of the viral genome, which can attenuate viruses and limits its application to laboratory strains. Thus, to understand infection kinetics and heterogeneity, a new type of approach is required.

Here, we develop "vRNP imaging at single-molecule resolution of unmodified negative-strand viruses" (VISUN), a broadly applicable approach for live-cell imaging of virus infection with single-vRNP resolution. VISUN not only allows imaging of negative-strand RNA viruses for the first time but also enables direct visualization of viral entry and vRNP localization, replication, and nuclear export with single-vRNP resolution. Moreover, VISUN does not require genome engineering, allowing real-time visualization of many viral variants and clinical samples. We apply VISUN to IAV to generate a single-cell map of the entire IAV infection cycle with unprecedented spatial and temporal resolution. Our analysis provides a comprehensive kinetic map of infection, reveals substantial heterogeneity among individual IAV infections, and identifies the key bottlenecks in infection that drive heterogeneous infection outcomes. Specifically, we find that heterogeneous viral gene expression signatures underlie heterogeneity in infection outcome and show that vRNP packaging defects, host cell division, and failed transcriptional activation together shape heterogeneous gene expression. Furthermore, by comparing viral gene expression signatures with infection history at the single-cell level, we determined the impact of loss of each viral genome segment in the context of natural infection. For example, loss of NS expression, but not polymerase subunit expression, severely delays replication onset, and defective expression of M or NS, but not HA, prevents vRNP nuclear export. In summary, our study identifies both the origins and consequences of infection heterogeneity, provides insights into viral gene function, and establishes a generally applicable technology to study virus infection.

RESULTS

Visualizing early IAV infection by single-molecule imaging

To map IAV infection cycle dynamics (Figure 1A), we aimed to develop a technology that would allow visualization of IAV infection in living cells with single-vRNP resolution. To label single vRNPs in living cells, we expressed a fluorescently tagged anti-NP nanobody (Nb^{NP}-GFP) fused to a nuclear localization signal (NLS) in human A549 cells and infected the cells with wild-type IAV (strain PR8) (Figure 1B).[17] Bright fluorescent foci were observed in individual cells by spinning-disk confocal microscopy after virus inoculation but not in mock-inoculated cells (Figures 1C, S1A, and S1B; Video S1), nor in cells pretreated with the IAV entry inhibitor bafilomycin A1 (BafA1) (Figure S1C).[18] At low multiplicity of infection (MOI), infected cells typically contained 7 or 8 spots, consistent with the expected number of vRNPs per virion (Figure S1D), whereas >8 foci were observed at higher MOI, allowing classification of cells as uninfected or infected with 1, 2, or >2 virions (Figures 1C and 1D). Because this approach enabled single-vRNP imaging of negative-strand RNA viruses, we refer to this method as "vRNP imaging at single-molecule resolution of unmodified negative-strand viruses" (VISUN). Combining VISUN with single-molecule fluorescence *in situ* hybridization (smFISH) labeling of vRNAs revealed that the large majority of VISUN foci represented vRNPs, with a small subset of VISUN spots likely representing encapsidated copy RNAs (cRNAs), positive-strand genome replication intermediates (Figures S1E–S1G). Labeling of vRNPs by VISUN did not substantially alter vRNP nuclear import or export rates (Figures S1H and S1I) or overall virus fitness (Figures 1E and 1F). In contrast, expression of Nb^{NP} without an NLS severely attenuated IAV infection, as reported previously[17,19] (Figure S1J), likely due to cytoplasmic sequestration of vRNPs by cytoplasmic Nb^{NP} upon viral entry. To ensure that VISUN spots represent full-length genome segments, rather than truncated defective interfering genomes (DIGs),[20–22] viruses were passaged a maximum of two times, and at low MOI before performing VISUN experiments, which minimized DIG formation (Figure S1K). To assess whether DIGs could, in principle, be detected using VISUN, we generated a virus stock though reverse genetics that exclusively contained a truncated HA segment of a length typical for DIGs (HA-DIG, 450 nt).[21,22] Using this virus stock, we determined that VISUN is sufficiently sensitive to detect DIGs (Figures S1L–S1N). VISUN could be successfully applied to a range of phylogenetically distant IAV isolates from human, swine, and avian origins, and was even successful for patient-derived virions (Figures 1G and S1O), enabling comparison of the infection cycle of different IAV strains and isolates. After vRNP entry, the number of VISUN spots in the nucleus typically remained constant for several hours, after which an increase in numbers was observed, indicative of vRNP replication (Figures 1H, 1I, and S2A). Spot number rapidly increased until too many spots were present to resolve individually, resulting in a diffuse nuclear signal (Figure 1H, referred to as "extensive vRNP replication"). The increase in the number of VISUN spots was matched by an increase in vRNAs, as detected by smFISH, indicating that it reflects *bona fide* genome replication (Figures S2B and S2C). At late stages of infection, cells harboring replicating virus often showed translocation of VISUN signal from the nucleus to the cytoplasm (Figure 1H [last time point] and 1J), reflecting vRNP nuclear export (Figures 1J, S2D, and S2E), which is known to occur late in infection to allow genome packaging into new virions at the plasma membrane. VISUN signal often accumulated in large foci near the cell periphery (Figure 1J, arrows), which may reflect sites of particle assembly. In conclusion, we have established VISUN as a single-molecule live-cell assay to visualize IAV infection, vRNP replication, and vRNP nuclear export. VISUN does not require genetic modification of IAV and can be applied to phylogenetically distant IAV variants. As such, VISUN provides a unique opportunity to study viral infection in single cells.

Please cite this article in press as: Rabouw et al., Live-cell single-vRNP imaging identifies viral gene expression signatures that shape influenza infection heterogeneity, Cell Systems (2025), https://doi.org/10.1016/j.cels.2025.101489

CellPress
OPEN ACCESS

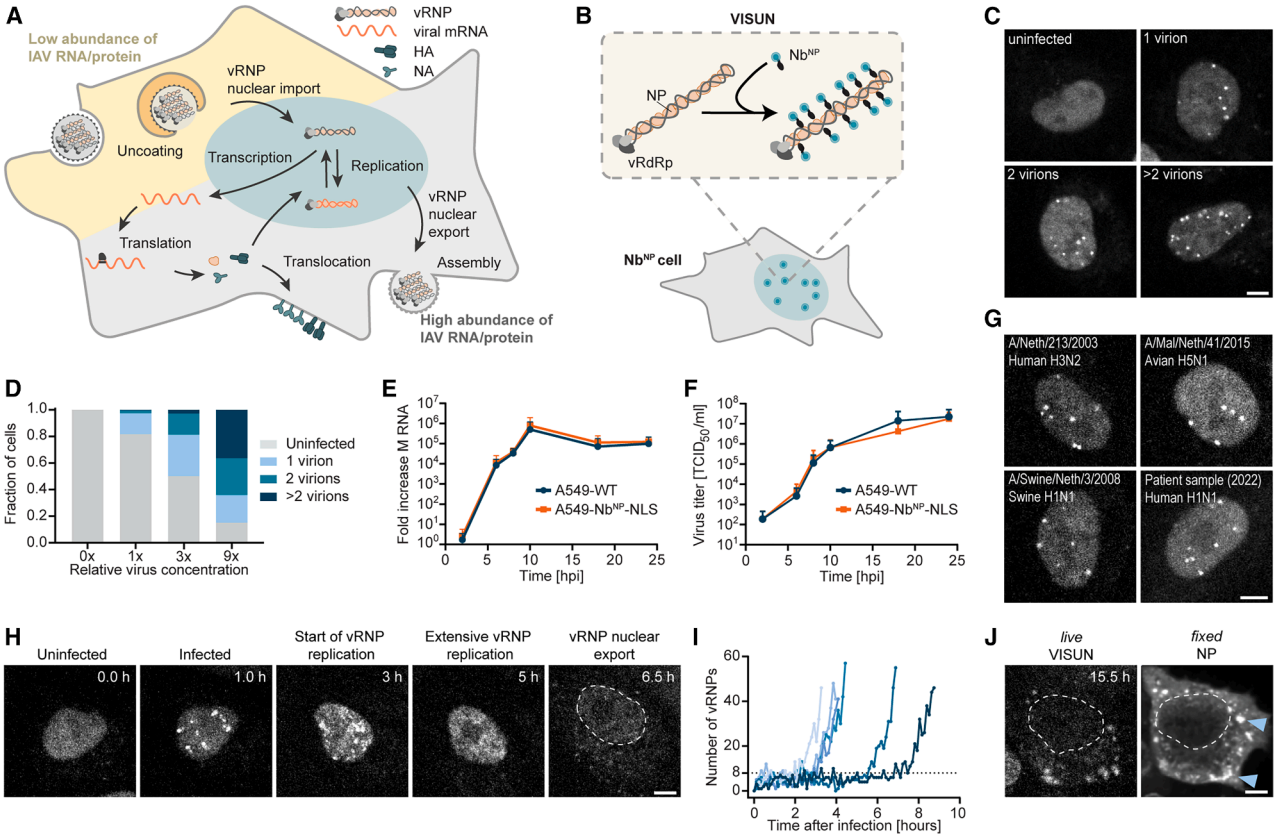

Figure 1. VISUN: A technology to image single IAV vRNPs in live cells

(A) Cartoon of the IAV infection cycle. Early (yellow shading) and late (gray shading) phases of infection are characterized by low and high abundance, respectively, of viral material in the cell.

(B) Cartoon of the VISUN single-vRNP imaging assay. Upon entry, fluorescently labeled Nb^{NP} molecules bind to multiple copies of NP present in vRNPs, locally enriching fluorescence signal. Nb^{NP} fluorescent spots in cells thus represent single vRNPs.

(C) Example images of A549-Nb^{NP}-NLS cells inoculated with IAV (strain PR8) at 1 hpi. Shown are examples of cells infected by 0, 1, 2, or >2 virions, inferred from the number of vRNPs.

(D) Quantification of the frequency of infections with 0, 1, 2, or >2 virions in A549-Nb^{NP}-NLS cells 1 hpi at different virus concentrations.

(E and F) Virus replication curves for the indicated cell lines as assessed by intracellular viral RNA quantification by qPCR (E) or infectious virus particle production as assessed by $TCID_{50}$ assay (F). Error bars indicate SD.

(G) Example images of A549-Nb^{NP}-NLS cells inoculated with the indicated IAV isolates, imaged at 1 hpi.

(H) Example images from a time-lapse movie of A549-Nb^{NP}-NLS cells inoculated with IAV. Images show indicated infection cycle phases as visualized by VISUN.

(I) Quantification of VISUN spot count over time in infected A549-Nb^{NP}-NLS cells. Every line represents a single cell. All traces were aligned *in silico* to the moment of first detection of VISUN spots. The expected value of eight vRNPs for a single-virion infection is indicated by the dashed line. Five representative cells are shown in which viral genome replication occurs.

(J) Last time point of the time-lapse movie shown in (H) showing nuclear export of vRNPs by VISUN (left) and NP immunofluorescence (IF) staining (right) of the same cell. Arrows highlight potential particle assembly sites.

(C, G, H, and J) Scale bars, 5 μm.

Mapping late-stage viral infection

To map the IAV infection cycle from beginning (vRNP entry) to end (viral progeny production), we aimed to develop a second, orthogonal approach to study infection progression during late stages of infection. We purified a fluorescently labeled Nb targeting the HA extracellular domain (Nb^{HA}) (Figure S3A)[23] and added it to the cell culture medium during long-term VISUN imaging (Figure 2A). Nb^{HA} labeled infected cells from 3 to 9 h post inoculation (hpi) (Figures 2B and 2C), allowing real-time, quantitative analysis of viral protein synthesis over the course of infection in single cells without genetic modification of the virus. Notably, most cells that underwent genome replication, as assessed by VISUN, showed strong Nb^{HA} labeling, whereas weak staining was found in a subset of infected cells in which no genome replication was observed, likely representing viral transcription in the absence of replication (Figures S3B and S3C). Nb^{HA} also successfully labeled single virions, which are coated by HA protein, both in purified virions and *in situ* in infected cell cultures, allowing real-time single-cell visualization of viral progeny production (Figures 2D, S3D, and S3E; Video S2). In summary, Nb^{HA} live-cell imaging is complementary to VISUN, and together these techniques can be used to map the kinetics and cell-to-cell heterogeneity of the IAV infection cycle from start to end.

Please cite this article in press as: Rabouw et al., Live-cell single-vRNP imaging identifies viral gene expression signatures that shape influenza infection heterogeneity, Cell Systems (2025), https://doi.org/10.1016/j.cels.2025.101489

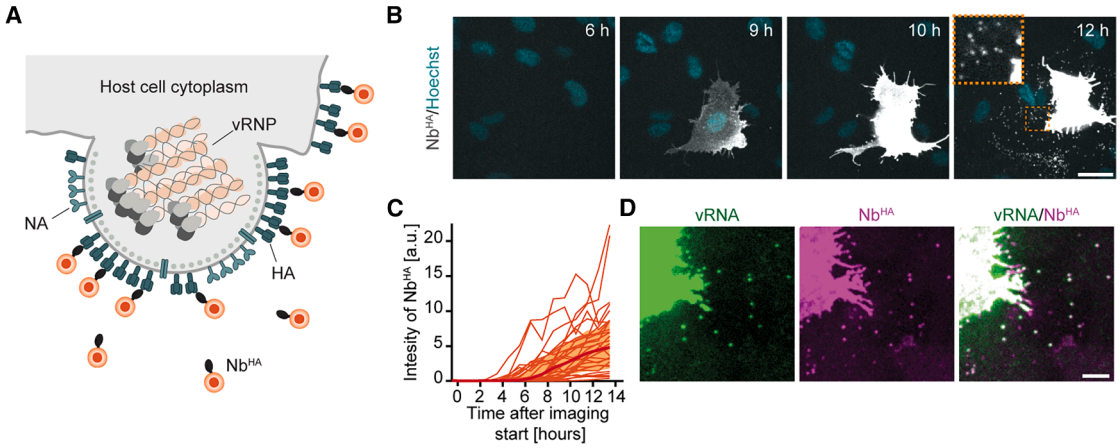

Figure 2. Nb^{HA} imaging reveals dynamics of viral protein synthesis and progeny production

(A) Cartoon illustrating the extracellular HA and progeny labeling method using the Nb^{HA}. Red circles indicate a fluorescent protein associated with the Nb^{HA}.

(B) Example images from a time-lapse movie of an IAV-infected cell labeled with Nb^{HA}. Orange dashed square indicates a zoom-in highlighting viral progeny release. Scale bar, 25 μm.

(C) Nb^{HA} intensity time traces of single cells that are infected with IAV undergoing vRNP replication. Replication was called using VISUN.

(D) Example images of an infected cell at 20 hpi stained with Nb^{HA} and smFISH probes targeting all vRNAs. The outline of the infected cell is visible along with multiple progeny virions (dual-color spots). Scale bar, 5 μm.

See also Video S2.

Single-cell viral infection kinetics

Having established VISUN and Nb^{HA} live-cell imaging technologies, we set out to generate a detailed map of IAV infection dynamics. Starting at vRNP entry, we first determined the time from virus inoculation to vRNP entry, which we found to be highly heterogeneous among cells, ranging from ~10 min to several hours (average, 190 ± 169 min) (Figure 3A). To identify the origin of heterogeneity in vRNP entry dynamics, we examined the timing of individual sub-steps in the viral entry pathway in more detail. IAV virions first undergo endocytosis by host cells, followed by virion fusion with endosomal membranes and nuclear import of vRNPs. To measure the time from endosomal uptake to nuclear entry, we synchronized virus entry by exploiting IAV's dependency on low pH for fusion (Figure S4).[24] After pH adjustment, vRNPs rapidly accumulated in the nucleus with a median time of 6.1 min (Figure 3A), which was much shorter than the median time of 140 min needed from virus inoculation to nuclear entry. Therefore, we conclude that the pre-fusion phase (host cell attachment and endocytosis) is the most time-consuming phase of vRNP entry. To dissect the kinetics of post-fusion vRNP release into the cytoplasm, we performed VISUN imaging with high temporal resolution after synchronized entry. Shortly after pH adjustment, a single bright, largely stationary spot appeared in many cells (median time to spot appearance, 1.3 min), which likely represents assemblies of all vRNPs in a bundle that are labeled by cytoplasmic Nb^{NP} immediately after endosomal fusion (Figures 3B and 3C), indicating that endosomal acidification and membrane fusion occur within minutes in this assay. From these bright foci, vRNPs split off in a step-by-step fashion (Figures 3B and 3D). Contradicting earlier studies had suggested that vRNPs were released from the vRNP bundle either individually[25] or in groups.[26] To resolve this question using our real-time single-vRNP imaging approach, we compared vRNP bundle intensity before and after the first VISUN spot split off from the bundle (see STAR Methods). This analysis revealed that, at least for IAV PR8, vRNPs were predominantly released as single vRNPs rather than as groups (Figure 3E). The entire vRNP unpacking process is relatively fast (median time of 1.1 min), indicating that this step is not a kinetic bottleneck in IAV infections (Figure 3F). Based on these results, we calculated the duration of intracellular transport of vRNPs from the endosomal release site to the nucleus to be ~5 min.

Our results provide a detailed map of IAV entry dynamics and identify viral attachment to host cells and the early stages of endocytosis as the major kinetic bottleneck in the viral entry process. We next aimed to map the kinetics of viral infection progression after vRNP nuclear entry. For this purpose, we performed long-term VISUN and Nb^{HA} imaging and determined the time between (1) vRNP entry and initiation of replication, (2) initiation of replication and vRNP nuclear export, (3) initiation of replication and HA accumulation, and (4) HA accumulation and virion production. Substantial cell-to-cell heterogeneity was observed for most steps of the infection cycle (Figures 3G–3K). Notably, the step from vRNP nuclear entry to initiation of replication (i.e., synthesis of sufficient viral polymerase and NP) took almost as long as the time from the first replication event to vRNP nuclear export, which encompasses synthesis of 10,000s–100,000s vRNAs[27] (3.3 vs. 5.2 h) (Figure 3I). These measurements reveal that preparation for the first replication rounds is relatively time consuming; however, once all components are in place, subsequent rounds of replication can occur rapidly, illustrating the highly exponential nature of replication during infection. The time from vRNP nuclear export to budding of progeny virions was short (~0.3 h), indicating that vRNP export from the nucleus is precisely timed during infection such that all components for packaging and virion budding have been prepared at the moment when vRNP nuclear export initiates (calculated from Figures 3I–3K). Late nuclear export of

Please cite this article in press as: Rabouw et al., Live-cell single-vRNP imaging identifies viral gene expression signatures that shape influenza infection heterogeneity, Cell Systems (2025), https://doi.org/10.1016/j.cels.2025.101489

CellPress
OPEN ACCESS

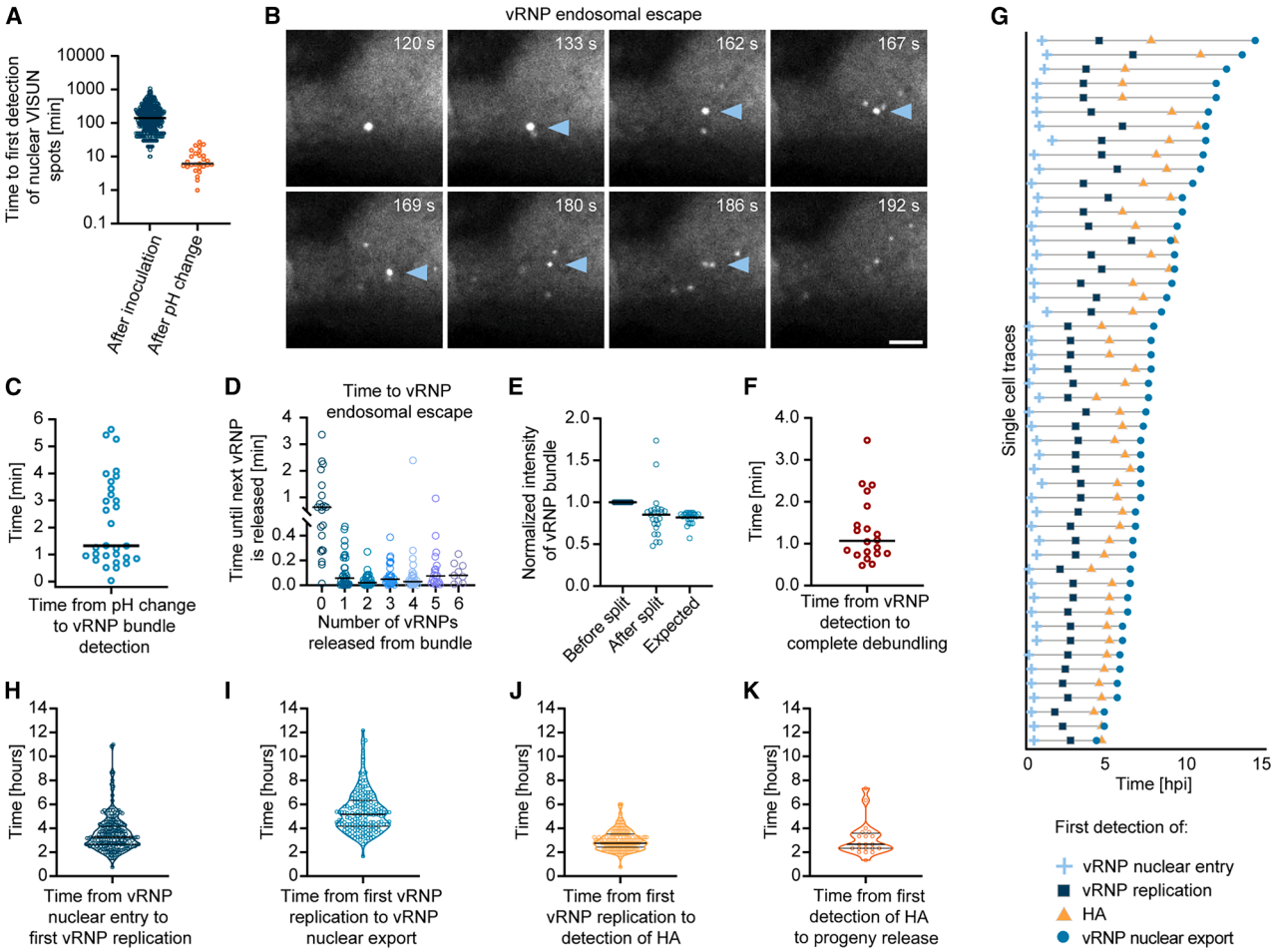

Figure 3. Mapping IAV infection cycle kinetics

(A) Quantification of the time of first nuclear detection of VISUN spots relative to the moment of inoculation (left) or to the moment of pH change (which induces virion-endosome fusion) (right).

(B) Example images of a time-lapse movie of IAV inoculated A549-Nb^{NP}-NLS cells showing vRNP cytoplasmic entry. Arrowheads indicate the slow-moving vRNP assembly, from which single vRNPs split off over time (dim spots). Scale bar, 5 μm. See also Video S3.

(C) Quantification of the time from pH adjustment to first detection of the vRNP bundle by VISUN.

(D) Quantification of the time until the next vRNP is released from the vRNP bundle, relative to the number of released vRNPs.

(E) Intensity of the vRNP bundle before and after the first VISUN spot splits off the bundle. Data are normalized to the intensity of the bundle before splitting. The expected intensity if a single vRNP splits off from the bundle is shown ("expected"). The expected intensity depends on the total number of vRNPs present in each bundle, which was assessed by counting the number of VISUN spots after debundling was complete.

(F) Quantification of the time between the first detection of the virion bundle and complete disassembly of the vRNP bundle. Dots represent single virions.

(G) Example single-cell viral infection cycle traces. The moment of vRNP nuclear entry, initiation of vRNP replication, first HA detection, and vRNP nuclear export are indicated. t = 0 indicates the moment of inoculation.

(H) Quantification of the time between vRNP nuclear entry and vRNP replication initiation.

(I) Quantification of the time between vRNP replication initiation and vRNP nuclear export.

(J) Quantification of the time between vRNP replication initiation and HA detection at the plasma membrane.

(K) Quantification of the time between HA detection at the plasma membrane and progeny virion release.

(A and C–F) Lines represent medians and dots single events. (H–K) Dots represent single cells.

See also Video S3.

vRNPs may allow maximal accumulation of vRNPs in the nucleus before packaging occurs to generate high numbers of new progeny. Together, these analyses establish a detailed single-cell kinetic map of infection progression and identify host cell attachment and endocytosis of virions, initiation of vRNP replication, and vRNP nuclear export as major kinetic bottlenecks in infection.

Infections progress through diverse pathways

A previous study showed that many infected cells fail to produce infectious virions, suggesting that one or more steps in the post-entry viral life cycle frequently fail.[15] Indeed, when we compared the viral titer as determined by VISUN, which assesses the number of virions that enter cells, with the titer as determined by a 50% tissue culture infectious dose ($TCID_{50}$) assay, which assesses the

Please cite this article in press as: Rabouw et al., Live-cell single-vRNP imaging identifies viral gene expression signatures that shape influenza infection heterogeneity, Cell Systems (2025), https://doi.org/10.1016/j.cels.2025.101489

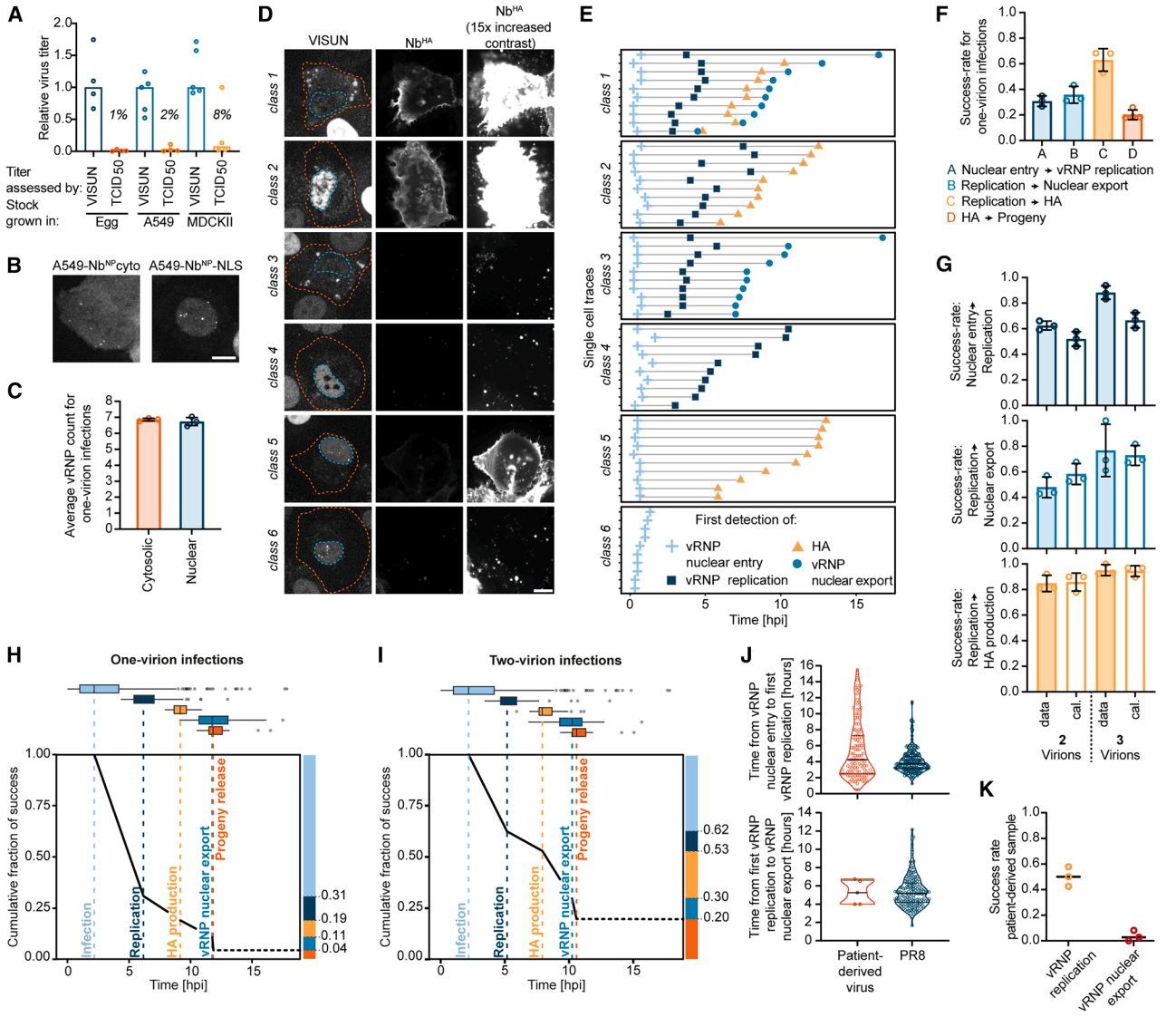

Figure 4. IAV infections abort at multiple steps in the viral infection cycle

(A) Viral titer for virus stocks produced in either A549 cells, MDCKII cells, or chicken eggs. The titer was determined either by VISUN, which detects vRNPs after entering the host cell nucleus, or by $TCID_{50}$, which detects only successful infections that cause a detectable cytopathic effect. Titers are shown relative to the median VISUN titer. Dots represent independent experiments.

(B) Example images of VISUN spots either in the cytoplasm of A549-Nb^{NP}cyto cells or in the nucleus of A549-Nb^{NP}-NLS cells, imaged at 1 hpi. Scale bar, 10 μm.

(C) Quantification of the number of vRNPs delivered into the cytoplasm or nucleus.

(D) Example images for six IAV infection phenotype classes. Orange dashed lines indicate cell outlines. Blue dashed lines indicate nuclear outlines. All Nb^{HA} images are also shown with 15-fold increased contrast (right). Note, that at these contrast settings, virions and fluorescent cell debris are also visible. Scale bar, 10 μm.

(E) Example single-cell infection cycle traces, which indicate the moment of nuclear vRNP detection, initiation of vRNP replication, first HA detection, and vRNP nuclear export. Each horizontal line represents a single cell.

(F) Quantification of the average fraction of one-virion infected cells in which vRNP replication, vRNP nuclear export, HA production, and progeny release are successful.

(G) Experimental (data) and calculated fraction of cells (cal.) with successful vRNP replication (top), vRNP nuclear export (middle), or HA production (bottom) for infections by 2 or 3 virions. Expected success rates were calculated assuming that each virion provided an independent chance of success (see STAR Methods).

(H and I) Graphs summarizing the kinetics and success rates of each infection cycle phase for one-virion (H) or two-virion (I) infections. Median times are indicated by dashed vertical lines, which are aligned to the end of the previous infection phase. The heterogeneity in infection phase duration is displayed as boxplots at the top of the graph. The expected success rate for progeny production for two-virion infections (I) could not be directly measured, as virion production can only be assigned to individual cells when using a very low MOI, which only results in infections with one virion. Therefore, the median time to virion production in two-virion infections was based on one-virion infections. The success rate of virion production was calculated assuming that each virion provided an independent chance of success.

(legend continued on next page)

Please cite this article in press as: Rabouw et al., Live-cell single-vRNP imaging identifies viral gene expression signatures that shape influenza infection heterogeneity, Cell Systems (2025), https://doi.org/10.1016/j.cels.2025.101489

number of virions that cause infections that produce infectious progeny (Figure 4A), we found a striking ~100-fold higher viral titer for vRNP entry, suggesting that the vast majority of infecting virions do not go on to produce viral progeny. The surprisingly low success rate of IAV infection progression was observed irrespective of the method of virus production (Figure 4A), confirming the validity of these results. To determine which steps in the infection cycle represent bottlenecks toward successful progeny formation, we first determined the efficiency of vRNP nuclear import, which revealed that vRNPs rarely, if ever, fail to translocate from the cytoplasm to the nucleus (Figures 4B and 4C). Thus, vRNP nuclear import does not represent a major bottleneck for successful infection. In contrast, using long-term VISUN and Nb^{HA} imaging, we found that every step after vRNP nuclear import that we assessed (genome replication, viral protein synthesis, vRNP nuclear export, and virion production) failed in a considerable fraction of infected cells, allowing us to distinguish six distinct classes of infection progression pathways (Figures 4D and 4E; Videos S4 and S5). Thus, the infection cycle of IAV contains numerous bottlenecks, explaining the low overall success rate of IAV infections. To assess viral infection dynamics and heterogeneity in a physiologically relevant context, we next repeated VISUN assays in airway epithelial organoids, primary untransformed cell cultures that accurately recapitulate cell types found in the human airway (Figure S5A).[28] We found very similar dynamics and success rates of replication (Figures S5B and S5C), as well as HA synthesis (Figures S5D and S5E), in airway organoids as compared with A549 cells, confirming the validity of our findings in A549 cells (Figure 4F).

VISUN provides a unique opportunity to group infected cells based on the number of infecting virions, allowing us to quantify the impact of virion number per infection on the success rate of each step in the infection cycle. This analysis revealed that multivirion infections have higher success rates than one-virion infections for every infection phase that was assessed (Figures 4F and 4G), with replication initiation being especially sensitive to virion number, suggesting that infections by multiple virions may enhance replication of each other (Figure 4G [top]). When summing the success rates for all individual steps, we calculated an overall success rate of one-virion infections of just 4% (Figure 4H), which corresponds well to the comparison in virus titer between VISUN and $TCID_{50}$ measurements (Figure 4A). The overall success rate of two-virion infections was increased by ~5-fold (Figure 4I), highlighting the large impact of the number of virions per infected cell on infection success and underscoring the importance of assessing the MOI for each infected cell when examining infection outcomes. Furthermore, a major advantage of VISUN over existing live-cell techniques is that it can be applied to unmodified viruses. We leveraged this unique advantage to map the infection cycle of patient-derived virions, which revealed similar heterogeneity in infection cycle pathways, with distinct success rates for individual steps in the infection cycle (Figures 4J and 4K).

Heterogeneous viral gene expression signatures underlie diverse infection pathways

The fact that the success rate of each step in viral infection is improved by co-infection with multiple virions suggests that abortive infections are caused, at least in part, by virion-intrinsic rather than cell-intrinsic heterogeneity. Virion-intrinsic heterogeneity can include heterogeneity in vRNP content or variable activity in transcription or replication. Whereas incoming vRNPs and vRNP replication are directly observable using VISUN, vRNP transcription is not. Therefore, to investigate whether transcriptional heterogeneity impacts infection progression, we combined VISUN and Nb^{HA} imaging with multiplexed smFISH to quantify the levels of mRNA species from all eight IAV segments, as well as three vRNA species (PB2, PB1, and NP) in individual cells (Figures 5A and S6; Video S6). smFISH allows detection of individual viral mRNA molecules and is therefore sensitive enough to detect primary viral transcription (i.e., transcription of the incoming vRNAs). Multiplexed smFISH revealed substantial differences in viral gene expression among infected cells, with between 0 and 8 different viral genome segments being transcribed and with expression levels differing by several orders of magnitude (Figures 5B and 5C). Unsupervised clustering of the gene expression data yielded 10 distinct clusters of cells (Figures 5C, 5D, and S7A). Cluster 1 corresponds to cells lacking detectable expression of any viral genome segment, which includes both uninfected cells and cells infected with IAV that did not produce any viral mRNAs (Figures 5C and S7B). Clusters 2–8 correspond to cells in which low viral mRNA levels (<100 mRNAs) were detected, with expression from only one or a few genome segments (Figure 5C), demonstrating that many infected cells transcribe a random, incomplete set of viral genome segments. The final two clusters, 9 and 10, consisted of cells with high levels of viral mRNA (Figure S7C). Cluster 9 cells have high levels of most but not all types of viral mRNAs, whereas most cluster 10 cells transcribe all eight genome segments at high levels (Figure 5C). From this analysis, we conclude that in the large majority of infected cells, most genome segments are transcriptionally silent.

To understand how heterogeneous viral gene expression impacts infection progression, we computed single-cell viral progression scores based on viral mRNA levels, as well as vRNA levels and localization, and assessed the impact of distinct viral gene expression signatures on infection progression (Figures 5E, 5F, and S7D–S7G). This approach allowed us to examine infections in which seven of the eight segments were transcribed, which effectively represent naturally occurring "single-gene knockouts," uniquely allowing assessment of the function of individual genome segments in infection progression. Studying such single-gene knockouts is difficult using genetic approaches because most IAV genes are essential for virion production. Analysis of single-gene knockouts revealed that lack of expression of the segments that are not essential for replication (HA, NA, M, and NS) had only a minor effect on the viral progression

(J) Quantification of the time between inoculation and initiation of replication (top) or between initiation of replication and nuclear export of vRNPs (bottom) in cells infected with patient-derived IAV (left) or PR8 (right).
(K) Success rates of vRNP replication (in infected cells) and vRNP nuclear export (in cells with replicating virus) in cells inoculated with patient-derived IAV.
(C, F, G, and K) Dots represent average values from independent experiments. Error bars represent SDs.
See also Videos S4 and S5.

Please cite this article in press as: Rabouw et al., Live-cell single-vRNP imaging identifies viral gene expression signatures that shape influenza infection heterogeneity, Cell Systems (2025), https://doi.org/10.1016/j.cels.2025.101489

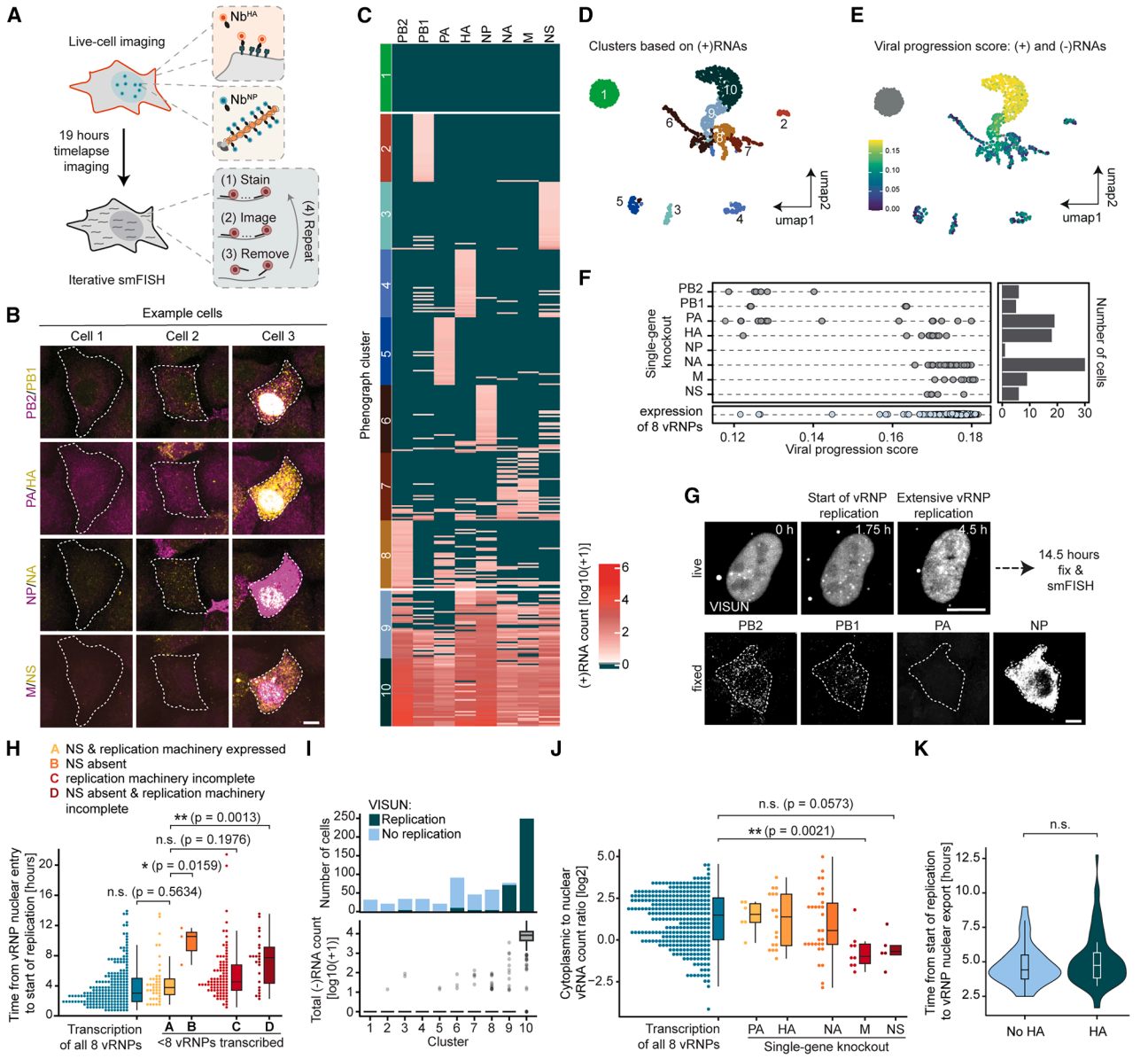

Figure 5. Abortive infections are caused by gene expression defects

(A) Schematic of the experimental procedure combining VISUN and Nb^{HA} imaging with fixed-cell multiplexed smFISH.

(B) Example images of multiplexed smFISH for three cells with varying levels of different viral mRNAs. Scale bar, 10 μm.

(C) Heatmap of mRNA levels for all eight viral genome segments. Each horizontal line represents one cell. Cells are grouped based on phenograph clusters (see D and Figures S7A–S7C). 40 randomly selected cells are shown for each cluster.

(D) Uniform manifold approximation and projection (UMAP) computed on mRNA levels for all eight viral genome segments, colored according to phenograph cluster. Cluster numbers, also used in (C) and (I), are shown.

(E) The viral progression score was calculated for each cell (Figures S7D–S7F) and projected onto the UMAP representation.

(F) Viral progression score of cells transcribing seven out of eight vRNPs, grouped based on which genome segment is transcriptionally silent. The inactive segment is indicated on the *y* axis. Number of cells in each group is shown on the right. Cells for which all eight genome segments are expressed are shown at the bottom.

(G) Example images of live-cell VISUN (top) and smFISH of the same cell (bottom) for a cell that shows IAV replication but lacks expression of the PA segment. Scale bars, 10 μm.

(H) Time between inoculation and first vRNP replication for cells that either express all four viral proteins needed for replication (PB1, PB2, PA, and NP) and NS, or lack expression of one or several of these proteins. Statistical significance was determined through a one-way ANOVA with Dunnett post-hoc test.

(I) Fraction of cells showing replication as assessed by VISUN (top), as well as total vRNA count (bottom) for cells in each phenograph cluster. Note that boxplots are not visible for clusters 1–9 (only outliers are visible), as the majority of cells in these clusters have very low vRNA count.

(legend continued on next page)

Please cite this article in press as: Rabouw et al., Live-cell single-vRNP imaging identifies viral gene expression signatures that shape influenza infection heterogeneity, Cell Systems (2025), https://doi.org/10.1016/j.cels.2025.101489

score (Figure 5F). Infections lacking expression of NP, PB2, PB1, or PA typically progress less far in infection (Figure 5F). The total number of infected cells in which all segments were transcribed except either NP, PB2 or PB1 was low, likely because infections lacking one of these segments arrest during very early infection, even before the other segments are transcribed sufficiently for detection (~>10 transcripts). Remarkably, some PB1, PB2, and especially PA single-gene knockout cells were identified with a relatively high viral progression score (Figure 5F). Consistently, some cells that were devoid of one of the polymerase subunit mRNAs showed unambiguous vRNP replication by VISUN (Figures 5G and 5H), indicating that limited genome replication can occur in the absence of expression of subunits of the replication machinery. Infected cells lacking polymerase subunit mRNAs were highly enriched in cluster 9 (Figures 5I and S8A–S8C). These cells often showed limited levels of replication, revealing that lack of *de novo* synthesis of the viral polymerase complex results in a block of viral progression after initial replication (Figure 5I, bottom). These results are surprising, as they differ from previous work, which suggested that even initiation of vRNP replication requires a second copy of the polymerase complex, likely created through *de novo* viral protein synthesis.[29,30] Limited replication as observed by VISUN does not exclusively reflect vRNA-to-cRNA replication, because vRNA amplification was also observed in cells lacking replication subunits (Figure S8D). Earlier studies have shown that NS2 promotes replication over transcription.[9,31] Although we had only a few NS knockout infections in our data, we nonetheless found that cells lacking NS mRNAs had increased mRNA/vRNA ratios (Figure S8E). Remarkably, lack of NS expression also resulted in a substantial delay in initiating replication, to a greater extent than lack of polymerase subunits (Figure 5H). Thus, our live-cell analyses expand on previous reports[9,31] by revealing that *de novo* synthesis of NS proteins may constitute a timer that controls the switch from transcription to the first round of replication.

We similarly assessed which viral genes play a role in vRNP nuclear export. We examined infected cells with a viral progression score of >0.15, the score that corresponds to the range at which vRNP nuclear export typically occurs (Figure S8F). Since insufficient numbers of infected cells (<5) lacking PB2, PB1, and NP reached this stage of viral infection progression—likely because of reduced replication efficiency—these viral genes were excluded from this analysis. A lack of M or NS expression impaired vRNP export, consistent with previous reports,[32–35] whereas a lack of HA, NA, or PA did not significantly affect vRNP export (Figure 5J). Our finding that HA is not important for vRNP nuclear export contradicts earlier reports showing that HA buildup at the plasma membrane is needed to trigger vRNP nuclear export.[36] To confirm our findings, we examined the timing of vRNP nuclear export in infected cells with or without HA expression and found that vRNP nuclear export occurred at similar times (Figure 5K). To exclude the possibility that HA at intracellular membranes (which is not detected by Nb^{HA}) triggered vRNP nuclear export, we examined HA mRNA expression and Nb^{HA} staining in the same cells. This analysis revealed that almost all cells lacking cell-surface HA also lacked HA mRNA and therefore did not contain intracellular HA protein (Figure S8G), confirming that HA protein accumulation does not impact vRNP nuclear export. In summary, these results show that most infected cells show viral gene expression defects and that distinct gene expression signatures underlie different types of infection progression failures.

Mechanisms of gene expression heterogeneity

We next investigated the mechanisms underlying heterogeneous gene expression signatures. Absence of mRNA expression could be due to missing genome segments, which, in turn, could be caused either by failures in vRNP packaging,[13,37,38] or, potentially, by degradation of vRNPs during infection.[39] Analysis of cells without viral replication revealed that vRNP number remained constant over time, suggesting that vRNP degradation is rare and therefore unlikely to contribute to the observed absence of vRNPs (Figure 6A). To assess the extent to which genome segment packaging defects could explain the observed lack of viral mRNA expression in infected cells, we quantified the frequency of missing genome segments in individual virions by smFISH. Genome segments were absent from virions at frequencies ranging from 8% to 27% (Figures 6B and 6C), consistent with previous reports.[13,37,38] Based on our smFISH measurements, we calculated that virions contain, on average, ~7 genome segments, a value similar to the average number of vRNPs per cell as determined by VISUN (6.7 vRNPs), confirming that VISUN spot count accurately reflects genome segment number per virion. To assess whether missing segments are randomly distributed among virions, we compared the expected number of vRNPs per virion, assuming that missing genome segments were randomly distributed across virions (i.e., vRNP number per virion follows a Poisson distribution), with the actual number of vRNPs per virion as determined by VISUN. We observed a broader distribution in vRNP number in the experimental data and an increased frequency of correctly packaged virions (8 vRNPs) (Figure 6D), explaining the origin of the highly diverse vRNP number per infected cell, which we observed in both PR8 and patient-derived virions (Figure S9A). These results suggest that vRNP packaging occurs in a cooperative manner. Cooperative packing of vRNP bundles might be explained by vRNP-vRNP interactions within a vRNP bundle that provide increasing bundle stability with increasing numbers of vRNPs in the bundle.[40,41] Besides packaging defects as a cause of missing genome segments, long-term time-lapse imaging of infection revealed that genome segments can also be lost during host cell division (Figure 6E). Quantification of vRNP numbers showed that both daughter cells after cell division receive approximately half of the vRNPs originally present in the mother cell (Figure 6F), indicating that vRNPs are segregated

(J) Ratio between cytoplasmic and nuclear staining intensity of (−)RNAs for single-gene knockout infections. Cells were only included if they have an infection progression score indicating that the infection is sufficiently progressed that vRNP nuclear export could occur (>0.15, see Figure S8F). Statistical significance was determined through a one-way ANOVA with Dunnett post-hoc test.

(K) Violin plots showing the time from vRNP replication initiation to vRNP nuclear export, as determined with VISUN, for cells either expressing or lacking HA, as determined by Nb^{HA} live-cell imaging.

(F, H, and J) Dots represent single cells.

Please cite this article in press as: Rabouw et al., Live-cell single-vRNP imaging identifies viral gene expression signatures that shape influenza infection heterogeneity, Cell Systems (2025), https://doi.org/10.1016/j.cels.2025.101489

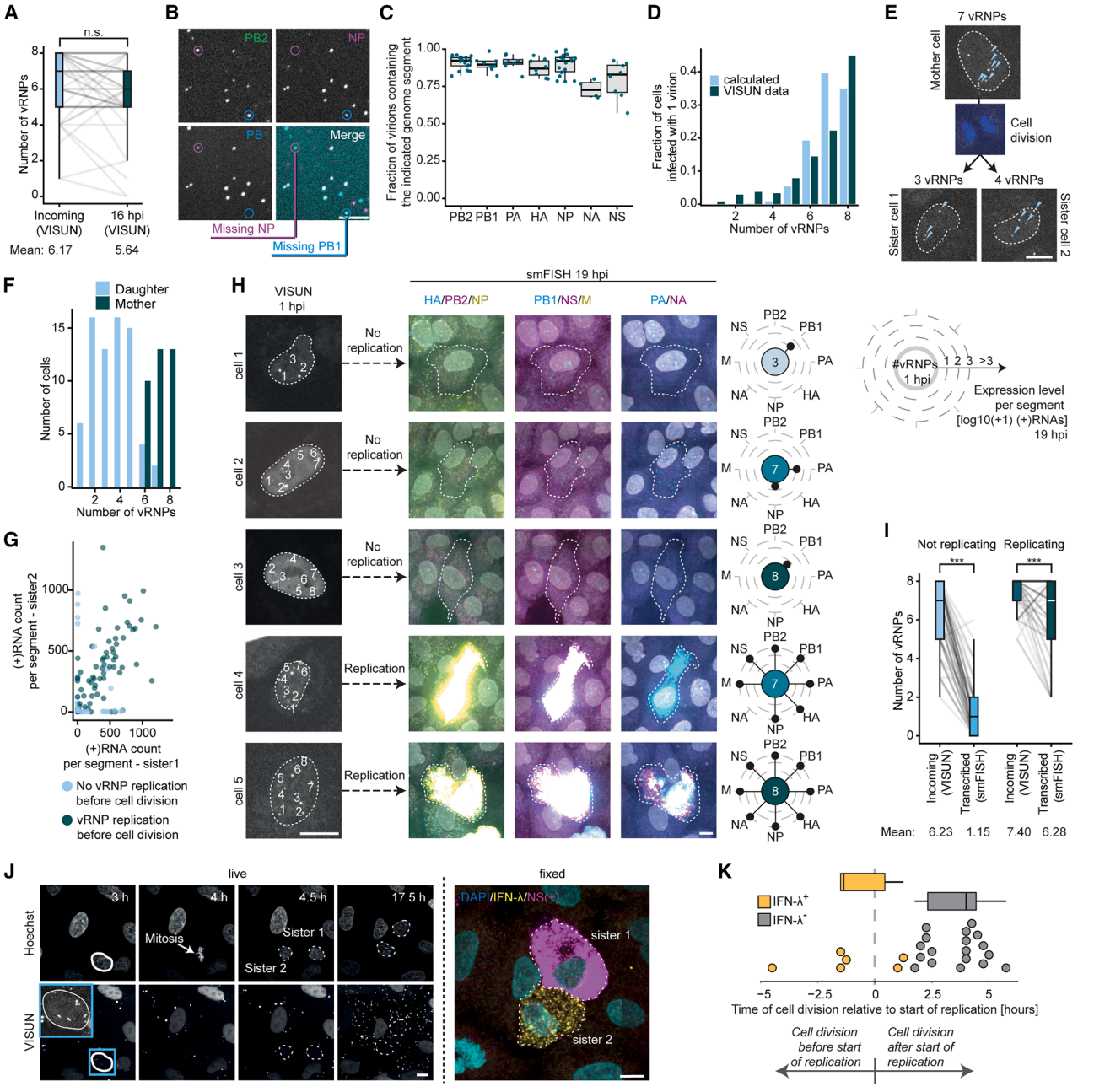

Figure 6. Mechanisms underlying viral gene expression defects and host cell response

(A) Boxplots showing the number of vRNPs per cell, as assessed by VISUN, for cells infected by a single virion in which no vRNP replication is observed. vRNP number was assessed for the same cells at both 1 and 16 hpi. Lines between boxplots link individual cells in both analyses. Slight variations in spot number at early and late time points are likely due to technical noise in measurements. Statistical significance was determined using a two-sided *t* test.

(B and C) IAV virions were spotted on glass and vRNAs were detected by smFISH. Representative images (B) and quantification (C) are shown. Note that genome segment M is missing from this analysis due to low signal of smFISH probes. Scale bar, 5 μm. Dots in (C) represent single fields of view.

(D) The number of vRNPs per virion determined experimentally by VISUN is shown (dark blue bars). Predicted distribution based on the frequency that each segment was absent from virions and assuming that missing segments are randomly distributed over virions is also shown (light blue bars).

(E) Example images of a VISUN movie for a cell undergoing cell division. DNA is stained with Hoechst. Scale bar, 10 μm.

(F) Quantification of the number of vRNPs per cell before and after cell division.

(G) Comparison of mRNA expression levels between two sister cells after cell division. Each dot represents the expression levels of a single genome segment.

(H) Example images of VISUN at 1 hpi and smFISH at 19 hpi for the same cells. Plots on the right show the number of vRNPs at 1 hpi in the center and mRNA expression levels at 19 hpi for each segment in the corresponding cell, shown as circular lollipop chart. Scale bar, 10 μm.

(legend continued on next page)

Please cite this article in press as: Rabouw et al., Live-cell single-vRNP imaging identifies viral gene expression signatures that shape influenza infection heterogeneity, Cell Systems (2025), https://doi.org/10.1016/j.cels.2025.101489

randomly during mitosis, creating two host cells with "viral aneuploidy." Viral aneuploidy was especially prevalent when replication had not yet occurred at the moment of host cell division (Figure 6G). Taken together, these results indicate that missing genome segments, caused either by packaging defects or vRNP segregation during mitosis, contribute to gene expression failure.

As described above, infected cells often lack genome segments, containing an average of ~7 out of eight genome segments. However, many infected cells express fewer than 2 genome segments, suggesting that defects other than missing genome segments contribute to the lack of viral gene expression (Figure 5C). To uncover the origin of the discrepancy between vRNP number and the number of expressed mRNAs, we compared the number of incoming vRNPs with the number of transcribed mRNAs in the same cells, for cells with or without replication. This analysis showed that many genome segments were transcriptionally silent, especially in cells without vRNP replication (Figures 6H, 6I, and S9B). Together, our results show that defective viral gene expression underlies most instances of abortive infection, and that the resulting diversity in gene expression signatures underlie heterogeneous infection cycle pathways. Furthermore, we find that defective viral gene expression is predominantly caused by transcriptional defects and, to a lesser extent, by missing vRNPs, which is caused either from packaging defects or unequal segregation of vRNPs during host cell division. We finally asked whether defects in viral gene expression affect the host cell antiviral response. Typically, only a small fraction of host cells induces expression of antiviral genes (e.g., interferons [IFNs]) in response to IAV infection.[11,42–44] Previous work identified the viral protein NS1 as the main antagonist of the antiviral response,[11,42–44] but how expression levels of NS1, as well as those of other viral genes, relate to antiviral response activation during infection of wild-type IAV has not been resolved. We found that IFN-λ, an antiviral gene that is upregulated in response to viral infection,[45,46] was exclusively expressed in cells with high viral mRNA expression (>100 total viral mRNAs) (Figures S10A and S10B), consistent with a recent report showing that viral load correlates positively with antiviral gene expression.[44] Focusing on infected cells with at least 100 viral mRNAs, we found that only 7% of these infected cells had activated IFN-λ transcription (Figure S10B), demonstrating highly efficient suppression of antiviral gene expression by wild-type IAV. Almost all IFN-λ-expressing host cells showed low or undetectable NS segment expression (Figure S10C), demonstrating that NS expression failure was a prerequisite for host innate immune activation during natural infection. A similar effect was not apparent for PB2 mRNA expression, despite the fact that PB2 has also been implicated as a potential immune antagonist (Figure S10C).[47–49]

Lack of NS expression alone, however, was insufficient to induce IFN-λ expression, even in cells with >100 mRNAs expressed (Figure S10C, lower left quadrant). VISUN imaging showed that a lack of IFN-λ expression in NS-negative cells typically coincided with lower rates of viral genome replication (Figure S10D). These data suggest that extensive replication is another prerequisite for activating antiviral responses. Finally, we found in our live-cell imaging data that cells undergoing mitosis within several hours of infection often showed one daughter cell with high IFN-λ expression (Figures 6J and 6K), which coincided with an absence of NS expression, indicating that the NS segment was lost in that daughter cell due to viral aneuploidy induced by host cell division. Thus, viral aneuploidy caused by mitosis could potentially affect the spread of IAV infections by inducing tissue-wide antiviral responses. Together, these data reveal how replication dynamics and viral gene expression defects shape antiviral response activation and identify viral aneuploidy induced by host cell division as an additional trigger for antiviral response activation.

DISCUSSION

In this study, we developed two complementary techniques, VISUN and Nb^{HA} imaging, that allow real-time visualization of the IAV infection cycle, from vRNP release into the cytoplasm through nuclear entry, replication, vRNP nuclear export, and virion production. Using these techniques, we generated a comprehensive single-cell kinetic map of the IAV infection cycle. We find that the vast majority of infections by single viral particles (~96%) fail to produce viral progeny due to failures at multiple distinct steps in the infection cycle. By combining live-cell analysis with multiplexed smFISH, we show that defective viral gene expression underlies aborted infections. We identify three major pathways that cause heterogeneous viral gene expression: vRNP packaging defects, defective transcriptional activation of vRNPs, and viral aneuploidy caused by host cell division. Loss of expression of individual viral genes, which occurs naturally in a heterogeneous population of infected cells, provided a unique opportunity to study viral gene function, including essential viral genes that cannot be knocked out genetically. Using these single-gene knockouts, we identify specific gene expression signatures associated with failures at different infection stages, shedding light on viral protein function. Our comprehensive infection map, which includes timing and success rates of vital steps in the viral life cycle, will provide a benchmark for studies detailing other IAV variants with varying pathogenicity and host range, as well as viral mutants and clinical isolates. Our data will help us understand how genetic evolution of viruses affects infection phenotypes and how host range and cell tropism, critical parameters for understanding viral evolution,

(I) Boxplots showing the number of vRNPs per cell, as assessed by VISUN, for cells infected by a single virion at 1 hpi (incoming), either for cells that do or do not show replication. The number vRNPs that show mRNA expression (transcribed) is shown for the same cells. Lines between boxplots link individual cells in both analyses. Statistical significance was determined using a two-sided *t* test.
(J) Example images of a time-lapse movie of an infected cell that underwent cell division after viral entry. The two sister cells after fixation and smFISH staining for IFN-λ and NS(+) are shown in the right. Scale bar, 10 μm.
(K) IFN-λ expression in relation to the timing of cell division and vRNP replication, as assessed by live-cell imaging. Only infections initiated by a viral particle that contained the NS segment are plotted. Viral particles were called NS-positive if one or both of the sister cells stained positive for the NS mRNA by smFISH at 19 hpi. Dots represent single cells.

Please cite this article in press as: Rabouw et al., Live-cell single-vRNP imaging identifies viral gene expression signatures that shape influenza infection heterogeneity, Cell Systems (2025), https://doi.org/10.1016/j.cels.2025.101489

spread, and pathogenicity, are affected by viral genotypes. Moreover, our approach can help understand how antiviral therapeutics and live attenuated vaccines function and may even be applicable in a diagnostic setting to detect IAV within minutes after sample collection.

Advantages of VISUN over existing techniques

Virus infection is a highly dynamic and heterogeneous process, and single-cell, real-time measurements are critical for gaining a complete understanding of the viral infection cycle. In this study, we introduce VISUN and Nb^{HA} imaging, which offer a unique combination of advantages over existing technologies used to study the IAV infection cycle, including the previously reported VIRIM technology.[16] First, the live-cell capability of VISUN combined with Nb^{HA} imaging provides an opportunity to map infection cycle kinetics and identify kinetic bottlenecks in infection. Live-cell approaches uniquely allow visualization of both early and late infection in the same cells, which is important for understanding how early infection heterogeneity impacts infection progression and outcome. Second, in contrast to VIRIM, VISUN does not require translation of the viral genome for visualization, which has several major advantages, including the ability to study the large and clinically important group of negative-strand RNA viruses, the ability to study viral entry and replication, and the ability to identify inactive vRNPs, which is critical for understanding infection bottlenecks. Third, the single-vRNP detection sensitivity of VISUN allows study of early infection, before sufficient viral protein and RNA are present in cells for detection with traditional assays. The highly sensitive detection afforded by VISUN can be leveraged to study the important process of viral tropism and host range for IAV isolates, by unambiguously distinguishing defects in viral entry from subsequent defects in viral replication. It is important to note that although VISUN provides single-vRNP sensitivity during early infection, single vRNPs cannot be resolved during late-stage infection, when vRNP numbers are very high. Nonetheless, several key steps in late-stage infection can be observed using VISUN, including bulk vRNP nuclear export and formation of sites of high VISUN signal near the cell periphery, which may reflect sites of particle assembly. A final advantage of VISUN is that it does not require genetic modification of the virus, making VISUN directly applicable to thousands of clinically relevant avian, swine, and human IAV isolates for which reverse genetics systems are not available. When combining VISUN with viral genome sequencing, it will be possible to relate viral genotype to infection phenotype to elucidate how genetic changes that occur during viral evolution impact viral infection biology.

Heterogeneity in viral infection success

Previous reports have found that the particle-to-plaque-forming-units ratio for many viruses is >>1,[50,51] and that many IAV-infected cells fail to produce infectious progeny virions.[15] It remained incompletely understood, however, which infection phases constitute bottlenecks and by what mechanisms. Our quantitative data show that failure occurs at many distinct steps of the infection cycle. Several aspects of the IAV life cycle may make it especially vulnerable to infection failure. First, the segmented nature of the IAV genome makes the virus vulnerable to genome packaging defects. Indeed, previous studies demonstrated that virions can lack genome segments,[38,52] which likely underlie viral gene expression deficiencies observed in infected cells.[15,53] Inefficient genome packaging and the resulting lack of gene expression and abortive infection likely cause co-infections to improve infection success because of genome segment complementation, as observed previously[53] and in our study. In addition to genome packaging defects, we find that vRNPs can also be lost post-entry during host cell division, in a process we term viral aneuploidy. Whether viral aneuploidy plays a significant role in the context of natural infections remains to be determined, because airway epithelial cells are typically thought to be quiescent.[54,55] Viral aneuploidy may occur in other cell types, such as basal cells that undergo cell division and can become infected.[14] Furthermore, increased cell proliferation in the airway has been observed upon tissue damage caused by viral infection,[56] suggesting that viral aneuploidy through host cell division may occur *in vivo*. A second feature of negative-sense RNA viruses like IAV that makes them vulnerable to infection failure is the requirement for transcription to occur before viral protein production can ensue. We find that initial activation of transcription creates a bottleneck in infection, which halts most infections. Why transcriptional activation fails in many infected cells is an interesting open question. These virions may contain faulty viral polymerases, incorrectly assembled vRNP complexes, or vRNAs that are defective or damaged. Infections that successfully initiate transcription of all available genome segments generally progress further in infection, but many still stall at later stages, frequently due to the absence of one or more viral genome segments. Thus, the complexity of the IAV viral genome and its infection cycle creates numerous bottlenecks toward successful infection. It will be informative to compare PR8 infection progression with other viral strains and isolates to identify how viral gene mutations affect specific steps in the infection cycle. Our detailed characterization of the infection cycle of the PR8 strain in A549 cells provides a benchmark against which future studies using other IAV variants or cell types can be compared.

Uncovering viral protein function through naturally occurring single-gene knockout viruses

The ability to assess vRNP number and identity in single cells allowed identification of infected cells that lacked a single viral genome segment and simultaneously provided detailed information about infection progression and host cell responses. Using this approach, viral gene function could be studied, including essential viral genes that cannot be knocked out genetically. Our results confirm a number of previous observations, including that the NS and M segments are essential for vRNP nuclear export (Figure 5J)[32–35] and that NS plays a crucial role in innate immune evasion (Figures 6J and 6K).[43,44,57,58] However, our experiments also provide new insights, some of which contrast earlier studies; for example, our analysis shows that HA expression is not essential for vRNP nuclear export, despite earlier work suggesting that HA accumulation functions as the trigger that initiates vRNP nuclear export.[36] In addition, we show that replication initiation can occur in the absence of viral mRNAs encoding a polymerase subunit, contrary to the general belief that vRNP replication requires *de novo* synthesis of polymerase complexes.[29,30] Small amounts of free polymerase proteins could be brought along in the virion to support initial replication. Due to its simplicity of use and easy compatibility with different

culture systems (e.g., different cell types, culture conditions, or mutant virus strains), VISUN has potential for studying many aspects of IAV infection biology. The broad applicability of the VISUN approach is highlighted by a recent application of a similar technique to respiratory syncytial virus (RSV), another negative-strand RNA virus.[59] We therefore envision application of our approach to study many different aspects of infection biology in IAV and other negative-strand RNA viruses.

RESOURCE AVAILABILITY

Lead contact

Further information and requests for resources and reagents should be directed to and will be fulfilled by the lead contact, Marvin Tanenbaum (m.tanenbaum@hubrecht.eu).

Materials availability

Plasmids generated in this study have been deposited at Addgene (#242815 pHR-NbNP-AausFP1-GB1-NLS, #242816 pHR_NbNP_mStayGold_GB1, #242817 pHR-CD5-Nb^{HA}-mCherry, #242818 pHR-CD5-Nb^{HA}-sfGFP). Other unique reagents generated in this study are available from the lead contact with a completed materials transfer agreement.

Data and code availability

- Representative subsets of the raw data have been deposited at Mendeley data repository and are publicly available as of the date of publication. DOIs are listed in the key resources table.
- All original code has been deposited at Zenodo and is publicly available as of the date of publication. DOIs are listed in the key resources table.
- Any additional information required to reanalyze the data reported in this paper is available from the lead contact upon request.

ACKNOWLEDGMENTS

J.S., H.H.R., M.J.D.B., and M.E.T. are supported by a grant from the European Union (ERC, VirIm, 101044794). M.M. and M.E.T. are financially supported by the Oncode Institute, which is funded in part by the Dutch Cancer Society (KWF). T.M.B. and R.A.M.F. are supported by the NIAID/NIH contract HHSN272201400008C and EU4Health grant DURABLE (no. 101102733).

AUTHOR CONTRIBUTIONS

Conceptualization, H.H.R., J.S., M.M., and M.E.T.; data curation, H.H.R., J.S., J.P., M.M., and M.J.D.B.; formal analysis, H.H.R., J.S., M.M., M.J.D.B., J.P., and M.E.T.; funding acquisition, H.C., R.A.M.F., and M.E.T.; investigation, H.H.R., J.S., M.M., J.P., and A.F.M.D.; methodology, H.H.R., J.S., M.M., M.J.D.B., A.F.M.D., T.M.B., H.C., R.A.M.F., and M.E.T.; project administration, H.H.R., J.S., M.M., M.J.D.B., H.C., R.A.M.F., and M.E.T.; resources, M.M., M.J.D.B., A.F.M.D., T.M.B., H.C., R.A.M.F., and M.E.T.; software, M.M. and M.J.D.B.; supervision, H.H.R., H.C., R.A.M.F., and M.E.T.; validation, H.H.R., J.S., and M.M.; visualization, H.H.R., J.S., M.M., M.J.D.B., and M.E.T.; writing – original draft, H.H.R., J.S., M.M., and M.E.T.; writing – review and editing, H.H.R., J.S., M.M., A.F.M.D., T.M.B., H.C., R.A.M.F., and M.E.T.

DECLARATION OF INTERESTS

H.C. was head of Pharma Research and Early Development at Roche in Basel and is an inventor on several patents related to organoid technology. His full disclosure is available at www.uu.nl/staff/JCClevers/Additional.

STAR★METHODS

Detailed methods are provided in the online version of this paper and include the following:

- KEY RESOURCES TABLE
- EXPERIMENTAL MODEL AND STUDY PARTICIPANT DETAILS
  - Cell lines
  - IAV production
  - Clinical IAV samples
  - Human airway epithelial cell culture and imaging
- METHOD DETAILS
  - Design of Nb expression constructs
  - Generation of stable cell lines
  - Nb^{HA} harvesting
  - IAV growth curve analyses
  - $TCID_{50}$ assay
  - qPCR analysis of intracellular viral RNA
  - Drug treatments of cells
  - Cell culture for imaging
  - Live-cell imaging of viral entry
  - smFISH
  - Virion smFISH
  - Immunofluorescence (IF) staining
  - Microscopy
- QUANTIFICATION AND STATISTICAL ANALYSIS
  - Maximum intensity projection of z-slices
  - Automated processing of live-cell imaging data
  - Live-cell imaging analyses
  - Analysis of multiplexed smFISH

SUPPLEMENTAL INFORMATION

Supplemental information can be found online at https://doi.org/10.1016/j.cels.2025.101489.

Received: April 17, 2025
Revised: October 17, 2025
Accepted: December 10, 2025

REFERENCES

1. Morens, D.M., Taubenberger, J.K., and Fauci, A.S. (2009). The persistent legacy of the 1918 influenza virus. N. Engl. J. Med. *361*, 225–229. https://doi.org/10.1056/NEJMp0904819.
2. Taubenberger, J.K., and Morens, D.M. (2006). 1918 Influenza: the mother of all pandemics. Emerg. Infect. Dis. *12*, 15–22. https://doi.org/10.3201/eid1201.050979.
3. Azziz Baumgartner, E., Dao, C.N., Nasreen, S., Bhuiyan, M.U., Mah-E-Muneer, S., Al Mamun, A., Sharker, M.A.Y., Zaman, R.U., Cheng, P.Y., Klimov, A.I., et al. (2012). Seasonality, timing, and climate drivers of influenza activity worldwide. J. Infect. Dis. *206*, 838–846. https://doi.org/10.1093/infdis/jis467.
4. Zhang, B., Xu, S., Liu, M., Wei, Y., Wang, Q., Shen, W., Lei, C.Q., and Zhu, Q. (2023). The nucleoprotein of influenza A virus inhibits the innate immune response by inducing mitophagy. Autophagy *19*, 1916–1933. https://doi.org/10.1080/15548627.2022.2162798.
5. Noda, T., and Kawaoka, Y. (2010). Structure of influenza virus ribonucleoprotein complexes and their packaging into virions. Rev. Med. Virol. *20*, 380–391. https://doi.org/10.1002/rmv.666.
6. Perez, J.T., Varble, A., Sachidanandam, R., Zlatev, I., Manoharan, M., García-Sastre, A., and tenOever, B.R. (2010). Influenza A virus-generated small RNAs regulate the switch from transcription to replication. Proc. Natl. Acad. Sci. USA *107*, 11525–11530. https://doi.org/10.1073/pnas.1001984107.
7. Vreede, F.T., Jung, T.E., and Brownlee, G.G. (2004). Model suggesting that replication of influenza virus is regulated by stabilization of replicative intermediates. J. Virol. *78*, 9568–9572. https://doi.org/10.1128/JVI.78.17.9568-9572.2004.
8. Carrique, L., Fan, H., Walker, A.P., Keown, J.R., Sharps, J., Staller, E., Barclay, W.S., Fodor, E., and Grimes, J.M. (2020). Host ANP32A mediates

the assembly of the influenza virus replicase. Nature *587*, 638–643. https://doi.org/10.1038/s41586-020-2927-z.

9. Sun, J., Kuai, L., Zhang, L., Xie, Y., Zhang, Y., Li, Y., Peng, Q., Shao, Y., Yang, Q., Tian, W.X., et al. (2024). NS2 induces an influenza A RNA polymerase hexamer and acts as a transcription to replication switch. EMBO Rep. *25*, 4708–4727. https://doi.org/10.1038/s44319-024-00208-4.
10. Vreede, F.T., Chan, A.Y., Sharps, J., and Fodor, E. (2010). Mechanisms and functional implications of the degradation of host RNA polymerase II in influenza virus infected cells. Virology *396*, 125–134. https://doi.org/10.1016/j.virol.2009.10.003.
11. Russell, A.B., Elshina, E., Kowalsky, J.R., Te Velthuis, A.J.W., and Bloom, J.D. (2019). Single-Cell Virus Sequencing of Influenza Infections That Trigger Innate Immunity. J. Virol. *93*, e00500-19. https://doi.org/10.1128/JVI.00500-19.
12. Zath, G.K., Thomas, M.M., Loveday, E.K., Bikos, D.A., Sanche, S., Ke, R., Brooke, C.B., and Chang, C.B. (2024). Influenza A viral burst size from thousands of infected single cells using droplet quantitative PCR (dqPCR). PLoS Pathog. *20*, e1012257. https://doi.org/10.1371/journal.ppat.1012257.
13. Russell, A.B., Trapnell, C., and Bloom, J.D. (2018). Extreme heterogeneity of influenza virus infection in single cells. eLife *7*, e32303. https://doi.org/10.7554/eLife.32303.
14. Kelly, J.N., Laloli, L., V'Kovski, P., Holwerda, M., Portmann, J., Thiel, V., and Dijkman, R. (2022). Comprehensive single cell analysis of pandemic influenza A virus infection in the human airways uncovers cell-type specific host transcriptional signatures relevant for disease progression and pathogenesis. Front. Immunol. *13*, 978824. https://doi.org/10.3389/fimmu.2022.978824.
15. Brooke, C.B., Ince, W.L., Wrammert, J., Ahmed, R., Wilson, P.C., Bennink, J.R., and Yewdell, J.W. (2013). Most influenza a virions fail to express at least one essential viral protein. J. Virol. *87*, 3155–3162. https://doi.org/10.1128/JVI.02284-12.
16. Boersma, S., Rabouw, H.H., Bruurs, L.J.M., Pavlovič, T., van Vliet, A.L.W., Beumer, J., Clevers, H., van Kuppeveld, F.J.M., and Tanenbaum, M.E. (2020). Translation and Replication Dynamics of Single RNA Viruses. Cell *183*, 1930–1945.e23. https://doi.org/10.1016/j.cell.2020.10.019.
17. Schmidt, F.I., Hanke, L., Morin, B., Brewer, R., Brusic, V., Whelan, S.P.J., and Ploegh, H.L. (2016). Phenotypic lentivirus screens to identify functional single domain antibodies. Nat. Microbiol. *1*, 16080. https://doi.org/10.1038/nmicrobiol.2016.80.
18. Ochiai, H., Sakai, S., Hirabayashi, T., Shimizu, Y., and Terasawa, K. (1995). Inhibitory effect of bafilomycin A1, a specific inhibitor of vacuolar-type proton pump, on the growth of influenza A and B viruses in MDCK cells. Antivir. Res. *27*, 425–430. https://doi.org/10.1016/0166-3542(95)00040-s.
19. Hanke, L., Knockenhauer, K.E., Brewer, R.C., van Diest, E., Schmidt, F.I., Schwartz, T.U., and Ploegh, H.L. (2016). The Antiviral Mechanism of an Influenza A Virus Nucleoprotein-Specific Single-Domain Antibody Fragment. mBio *7*, e01569-16. https://doi.org/10.1128/mBio.01569-16.
20. Davis, A.R., Hiti, A.L., and Nayak, D.P. (1980). Influenza defective interfering viral RNA is formed by internal deletion of genomic RNA. Proc. Natl. Acad. Sci. USA *77*, 215–219. https://doi.org/10.1073/pnas.77.1.215.
21. Lui, W.Y., Yuen, C.K., Li, C., Wong, W.M., Lui, P.Y., Lin, C.H., Chan, K.H., Zhao, H., Chen, H., To, K.K.W., et al. (2019). SMRT sequencing revealed the diversity and characteristics of defective interfering RNAs in influenza A (H7N9) virus infection. Emerg. Microbes Infect. *8*, 662–674. https://doi.org/10.1080/22221751.2019.1611346.
22. Saira, K., Lin, X., DePasse, J.V., Halpin, R., Twaddle, A., Stockwell, T., Angus, B., Cozzi-Lepri, A., Delfino, M., Dugan, V., et al. (2013). Sequence analysis of in vivo defective interfering-like RNA of influenza A H1N1 pandemic virus. J. Virol. *87*, 8064–8074. https://doi.org/10.1128/JVI.00240-13.
23. Gaiotto, T., and Hufton, S.E. (2016). Cross-Neutralising Nanobodies Bind to a Conserved Pocket in the Hemagglutinin Stem Region Identified Using Yeast Display and Deep Mutational Scanning. PLoS One *11*, e0164296. https://doi.org/10.1371/journal.pone.0164296.
24. Caffrey, M., and Lavie, A. (2021). pH-Dependent Mechanisms of Influenza Infection Mediated by Hemagglutinin. Front. Mol. Biosci. *8*, 777095. https://doi.org/10.3389/fmolb.2021.777095.
25. Qin, C., Li, W., Li, Q., Yin, W., Zhang, X., Zhang, Z., Zhang, X.E., and Cui, Z. (2019). Real-time dissection of dynamic uncoating of individual influenza viruses. Proc. Natl. Acad. Sci. USA *116*, 2577–2582. https://doi.org/10.1073/pnas.1812632116.
26. Chou, Y.Y., Heaton, N.S., Gao, Q., Palese, P., Singer, R.H., and Lionnet, T. (2013). Colocalization of different influenza viral RNA segments in the cytoplasm before viral budding as shown by single-molecule sensitivity FISH analysis. PLoS Pathog. *9*, e1003358. https://doi.org/10.1371/journal.ppat.1003358.
27. Heldt, F.S., Kupke, S.Y., Dorl, S., Reichl, U., and Frensing, T. (2015). Single-cell analysis and stochastic modelling unveil large cell-to-cell variability in influenza A virus infection. Nat. Commun. *6*, 8938. https://doi.org/10.1038/ncomms9938.
28. Sachs, N., Papaspyropoulos, A., Zomer-van Ommen, D.D., Heo, I., Böttinger, L., Klay, D., Weeber, F., Huelsz-Prince, G., Iakobachvili, N., Amatngalim, G.D., et al. (2019). Long-term expanding human airway organoids for disease modeling. EMBO J. *38*, e100300. https://doi.org/10.15252/embj.2018100300.
29. York, A., Hengrung, N., Vreede, F.T., Huiskonen, J.T., and Fodor, E. (2013). Isolation and characterization of the positive-sense replicative intermediate of a negative-strand RNA virus. Proc. Natl. Acad. Sci. USA *110*, E4238–E4245. https://doi.org/10.1073/pnas.1315068110.
30. Fan, H., Walker, A.P., Carrique, L., Keown, J.R., Serna Martin, I., Karia, D., Sharps, J., Hengrung, N., Pardon, E., Steyaert, J., et al. (2019). Structures of influenza A virus RNA polymerase offer insight into viral genome replication. Nature *573*, 287–290. https://doi.org/10.1038/s41586-019-1530-7.
31. Robb, N.C., Smith, M., Vreede, F.T., and Fodor, E. (2009). NS2/NEP protein regulates transcription and replication of the influenza virus RNA genome. J. Gen. Virol. *90*, 1398–1407. https://doi.org/10.1099/vir.0.009639-0.
32. Brunotte, L., Flies, J., Bolte, H., Reuther, P., Vreede, F., and Schwemmle, M. (2014). The nuclear export protein of H5N1 influenza A viruses recruits Matrix 1 (M1) protein to the viral ribonucleoprotein to mediate nuclear export. J. Biol. Chem. *289*, 20067–20077. https://doi.org/10.1074/jbc.M114.569178.
33. Bui, M., Wills, E.G., Helenius, A., and Whittaker, G.R. (2000). Role of the influenza virus M1 protein in nuclear export of viral ribonucleoproteins. J. Virol. *74*, 1781–1786. https://doi.org/10.1128/jvi.74.4.1781-1786.2000.
34. O'Neill, R.E., Talon, J., and Palese, P. (1998). The influenza virus NEP (NS2 protein) mediates the nuclear export of viral ribonucleoproteins. EMBO J. *17*, 288–296. https://doi.org/10.1093/emboj/17.1.288.
35. Martin, K., and Helenius, A. (1991). Nuclear transport of influenza virus ribonucleoproteins: the viral matrix protein (M1) promotes export and inhibits import. Cell *67*, 117–130. https://doi.org/10.1016/0092-8674(91)90576-k.
36. Marjuki, H., Alam, M.I., Ehrhardt, C., Wagner, R., Planz, O., Klenk, H.-D., Ludwig, S., and Pleschka, S. (2006). Membrane Accumulation of Influenza A Virus Hemagglutinin Triggers Nuclear Export of the Viral Genome via Protein Kinase Cα-mediated Activation of ERK Signaling. J. Biol. Chem. *281*, 16707–16715. https://doi.org/10.1074/jbc.M510233200.
37. Nakatsu, S., Sagara, H., Sakai-Tagawa, Y., Sugaya, N., Noda, T., and Kawaoka, Y. (2016). Complete and Incomplete Genome Packaging of Influenza A and B Viruses. mBio *7*, e01248-16. https://doi.org/10.1128/mBio.01248-16.
38. Chou, Y.Y., Vafabakhsh, R., Doğanay, S., Gao, Q., Ha, T., and Palese, P. (2012). One influenza virus particle packages eight unique viral RNAs as shown by FISH analysis. Proc. Natl. Acad. Sci. USA *109*, 9101–9106. https://doi.org/10.1073/pnas.1206069109.
39. Schelker, M., Mair, C.M., Jolmes, F., Welke, R.W., Klipp, E., Herrmann, A., Flöttmann, M., and Sieben, C. (2016). Viral RNA Degradation and Diffusion Act as a Bottleneck for the Influenza A Virus Infection Efficiency.

PLoS Comput. Biol. *12*, e1005075. https://doi.org/10.1371/journal.pcbi.1005075.

40. Le Sage, V., Kanarek, J.P., Snyder, D.J., Cooper, V.S., Lakdawala, S.S., and Lee, N. (2020). Mapping of Influenza Virus RNA-RNA Interactions Reveals a Flexible Network. Cell Rep. *31*, 107823. https://doi.org/10.1016/j.celrep.2020.107823.
41. Noda, T., Sugita, Y., Aoyama, K., Hirase, A., Kawakami, E., Miyazawa, A., Sagara, H., and Kawaoka, Y. (2012). Three-dimensional analysis of ribonucleoprotein complexes in influenza A virus. Nat. Commun. *3*, 639. https://doi.org/10.1038/ncomms1647.
42. Sun, J., Vera, J.C., Drnevich, J., Lin, Y.T., Ke, R., and Brooke, C.B. (2020). Single cell heterogeneity in influenza A virus gene expression shapes the innate antiviral response to infection. PLoS Pathog. *16*, e1008671. https://doi.org/10.1371/journal.ppat.1008671.
43. Killip, M.J., Jackson, D., Pérez-Cidoncha, M., Fodor, E., and Randall, R.E. (2017). Single-cell studies of IFN-beta promoter activation by wild-type and NS1-defective influenza A viruses. J. Gen. Virol. *98*, 357–363. https://doi.org/10.1099/jgv.0.000687.
44. Vicary, A.C., Mendes, M., Swaminath, S., Lekbua, A., Reddan, J., Rodriguez, Z.K., and Russell, A.B. (2023). Maximal interferon induction by influenza lacking NS1 is infrequent owing to requirements for replication and export. PLoS Pathog. *19*, e1010943. https://doi.org/10.1371/journal.ppat.1010943.
45. Ramos, I., Smith, G., Ruf-Zamojski, F., Martínez-Romero, C., Fribourg, M., Carbajal, E.A., Hartmann, B.M., Nair, V.D., Marjanovic, N., Monteagudo, P.L., et al. (2019). Innate Immune Response to Influenza Virus at Single-Cell Resolution in Human Epithelial Cells Revealed Paracrine Induction of Interferon Lambda 1. J. Virol. *93*, e00559-19. https://doi.org/10.1128/JVI.00559-19.
46. Liu, Y.G., Jin, S.W., Zhang, S.S., Xia, T.J., Liao, Y.H., Pan, R.L., Yan, M.Z., and Chang, Q. (2024). Interferon lambda in respiratory viral infection: immunomodulatory functions and antiviral effects in epithelium. Front. Immunol. *15*, 1338096. https://doi.org/10.3389/fimmu.2024.1338096.
47. Yang, H., Dong, Y., Bian, Y., Xu, N., Wu, Y., Yang, F., Du, Y., Qin, T., Chen, S., Peng, D., et al. (2022). The influenza virus PB2 protein evades antiviral innate immunity by inhibiting JAK1/STAT signalling. Nat. Commun. *13*, 6288. https://doi.org/10.1038/s41467-022-33909-2.
48. Graef, K.M., Vreede, F.T., Lau, Y.F., McCall, A.W., Carr, S.M., Subbarao, K., and Fodor, E. (2010). The PB2 subunit of the influenza virus RNA polymerase affects virulence by interacting with the mitochondrial antiviral signaling protein and inhibiting expression of beta interferon. J. Virol. *84*, 8433–8445. https://doi.org/10.1128/JVI.00879-10.
49. Iwai, A., Shiozaki, T., Kawai, T., Akira, S., Kawaoka, Y., Takada, A., Kida, H., and Miyazaki, T. (2010). Influenza A virus polymerase inhibits type I interferon induction by binding to interferon beta promoter stimulator 1. J. Biol. Chem. *285*, 32064–32074. https://doi.org/10.1074/jbc.M110.112458.
50. Carter, M.J., and Mahy, B.W. (1982). Incomplete avian influenza virus contains a defective non-interfering component. Arch. Virol. *71*, 13–25. https://doi.org/10.1007/BF01315172.
51. Hirst, G.K., and Pons, M.W. (1973). Mechanism of influenza recombination. II. Virus aggregation and its effect on plaque formation by so-called noninfective virus. Virology *56*, 620–631. https://doi.org/10.1016/0042-6822(73)90063-9.
52. Noda, T., Murakami, S., Nakatsu, S., Imai, H., Muramoto, Y., Shindo, K., Sagara, H., and Kawaoka, Y. (2018). Importance of the 1+7 configuration of ribonucleoprotein complexes for influenza A virus genome packaging. Nat. Commun. *9*, 54. https://doi.org/10.1038/s41467-017-02517-w.
53. Jacobs, N.T., Onuoha, N.O., Antia, A., Steel, J., Antia, R., and Lowen, A.C. (2019). Incomplete influenza A virus genomes occur frequently but are readily complemented during localized viral spread. Nat. Commun. *10*, 3526. https://doi.org/10.1038/s41467-019-11428-x.
54. Ayers, M.M., and Jeffery, P.K. (1988). Proliferation and differentiation in mammalian airway epithelium. Eur. Respir. J. *1*, 58–80. https://doi.org/10.1183/09031936.93.01010058.
55. Pardo-Saganta, A., Law, B.M., Gonzalez-Celeiro, M., Vinarsky, V., and Rajagopal, J. (2013). Ciliated cells of pseudostratified airway epithelium do not become mucous cells after ovalbumin challenge. Am. J. Respir. Cell Mol. Biol. *48*, 364–373. https://doi.org/10.1165/rcmb.2012-0146OC.
56. Kumar, P.A., Hu, Y., Yamamoto, Y., Hoe, N.B., Wei, T.S., Mu, D., Sun, Y., Joo, L.S., Dagher, R., Zielonka, E.M., et al. (2011). Distal airway stem cells yield alveoli in vitro and during lung regeneration following H1N1 influenza infection. Cell *147*, 525–538. https://doi.org/10.1016/j.cell.2011.10.001.
57. Jia, D., Rahbar, R., Chan, R.W.Y., Lee, S.M.Y., Chan, M.C.W., Wang, B.X., Baker, D.P., Sun, B., Peiris, J.S.M., Nicholls, J.M., et al. (2010). Influenza virus non-structural protein 1 (NS1) disrupts interferon signaling. PLoS One *5*, e13927. https://doi.org/10.1371/journal.pone.0013927.
58. Kochs, G., García-Sastre, A., and Martínez-Sobrido, L. (2007). Multiple anti-interferon actions of the influenza A virus NS1 protein. J. Virol. *81*, 7011–7021. https://doi.org/10.1128/JVI.02581-06.
59. Ratnayake, D., Galloux, M., Boersma, S., Sizun, C., Sourimant, J., Lakerveld, A.J., Baars, M.J.D., Banerjee, R., Noerenberg, M., Dreier, B., et al. (2026). Pre-assembly of biomolecular condensate seeds drives RSV replication. Nature. https://doi.org/10.1038/s41586-025-10071-5.
60. Wijnakker, J.J.A.P.M., van Son, G.J.F., Krueger, D., van de Wetering, W.J., Lopez-Iglesias, C., Schreurs, R., van Rijt, F., Lim, S., Lin, L., Peters, P.J., et al. (2025). Integrin-activating Yersinia protein Invasin sustains long-term expansion of primary epithelial cells as 2D organoid sheets. Proc. Natl. Acad. Sci. USA *122*, e2420595121. https://doi.org/10.1073/pnas.2420595121.
61. R Core Team (2022). A Language and Environment for Statistical Computing (R Foundation for Statistical Computing).
62. Wickham, H. (2016). ggplot2: Elegant Graphics for Data Analysis (Springer-Verlag).
63. Wickham, H., François, R., Henry, L., Müller, K., and Vaughan, D. (2023). dplyr: A Grammar of Data Manipulation. https://dplyr.tidyverse.org/.
64. Chalfoun, J., Majurski, M., Blattner, T., Bhadriraju, K., Keyrouz, W., Bajcsy, P., and Brady, M. (2017). MIST: Accurate and Scalable Microscopy Image Stitching Tool with Stage Modeling and Error Minimization. Sci. Rep. *7*, 4988. https://doi.org/10.1038/s41598-017-04567-y.
65. Levine, J.H., Simonds, E.F., Bendall, S.C., Davis, K.L., Amir el, A.D., Tadmor, M.D., Litvin, O., Fienberg, H.G., Jager, A., Zunder, E.R., et al. (2015). Data-Driven Phenotypic Dissection of AML Reveals Progenitor-like Cells that Correlate with Prognosis. Cell *162*, 184–197. https://doi.org/10.1016/j.cell.2015.05.047.
66. McInnes, L., Healy, J., and Melville, J. (2020). UMAP: Uniform Manifold Approximation and Projection for Dimension Reduction. Preprint at arXiv. https://doi.org/10.48550/arXiv.1802.03426.
67. Angerer, P., Haghverdi, L., Büttner, M., Theis, F.J., Marr, C., and Buettner, F. (2016). destiny: diffusion maps for large-scale single-cell data in R. Bioinformatics *32*, 1241–1243. https://doi.org/10.1093/bioinformatics/btv715.
68. Street, K., Risso, D., Fletcher, R.B., Das, D., Ngai, J., Yosef, N., Purdom, E., and Dudoit, S. (2018). Slingshot: cell lineage and pseudotime inference for single-cell transcriptomics. BMC Genomics *19*, 477. https://doi.org/10.1186/s12864-018-4772-0.
69. Pachitariu, M., and Stringer, C. (2022). Cellpose 2.0: how to train your own model. Nat. Methods *19*, 1634–1641. https://doi.org/10.1038/s41592-022-01663-4.
70. Ershov, D., Phan, M.S., Pylvänäinen, J.W., Rigaud, S.U., Le Blanc, L., Charles-Orszag, A., Conway, J.R.W., Laine, R.F., Roy, N.H., Bonazzi, D., et al. (2022). TrackMate 7: integrating state-of-the-art segmentation algorithms into tracking pipelines. Nat. Methods *19*, 829–832. https://doi.org/10.1038/s41592-022-01507-1.
71. van der Walt, S., Schönberger, J.L., Nunez-Iglesias, J., Boulogne, F., Warner, J.D., Yager, N., Gouillart, E., and Yu, T.; scikit-image contributors (2014). scikit-image: image processing in Python. PeerJ *2*, e453. https://doi.org/10.7717/peerj.453.

72. Eichenberger, B.T., Zhan, Y., Rempfler, M., Giorgetti, L., and Chao, J.A. (2021). deepBlink: threshold-independent detection and localization of diffraction-limited spots. Nucleic Acids Res. *49*, 7292–7297. https://doi.org/10.1093/nar/gkab546.

73. Peng, T., Thorn, K., Schroeder, T., Wang, L., Theis, F.J., Marr, C., and Navab, N. (2017). A BaSiC tool for background and shading correction of optical microscopy images. Nat. Commun. *8*, 14836. https://doi.org/10.1038/ncomms14836.

74. Thévenaz, P., Ruttimann, U.E., and Unser, M. (1998). A pyramid approach to subpixel registration based on intensity. IEEE Trans. Image Process. *7*, 27–41. https://doi.org/10.1109/83.650848.

75. Sofroniew, N., Lambert, T., Bokota, G., Nunez-Iglesias, J., Sobolewski, P., Sweet, A., Gaifas, L., Evans, K., Burt, A., Doncila Pop, D., et al. (2024). napari: a multi-dimensional image viewer for Python (v0.5.4). Zenodo. https://doi.org/10.5281/zenodo.13863809.

76. Imbert, A., Ouyang, W., Safieddine, A., Coleno, E., Zimmer, C., Bertrand, E., Walter, T., and Mueller, F. (2022). FISH-quant v2: a scalable and modular tool for smFISH image analysis. RNA *28*, 786–795. https://doi.org/10.1261/rna.079073.121.

77. de Wit, E., Spronken, M.I.J., Bestebroer, T.M., Rimmelzwaan, G.F., Osterhaus, A.D.M.E., and Fouchier, R.A.M. (2004). Efficient generation and growth of influenza virus A/PR/8/34 from eight cDNA fragments. Virus Res. *103*, 155–161. https://doi.org/10.1016/j.virusres.2004.02.028.

78. Dayton, T.L., Alcala, N., Moonen, L., den Hartigh, L., Geurts, V., Mangiante, L., Lap, L., Dost, A.F.M., Beumer, J., Levy, S., et al. (2023). Druggable growth dependencies and tumor evolution analysis in patient-derived organoids of neuroendocrine neoplasms from multiple body sites. Cancer Cell *41*, 2083–2099.e9. https://doi.org/10.1016/j.ccell.2023.11.007.

79. Liu, M.Y., Chen, B., Borji, M., Garcia de Alba Rivas, C., Dost, A.F.M., Moye, A.L., Movval Abdulla, N., Paschini, M., Rollins, S.D., Wang, R., et al. (2024). Human Airway and Alveolar Organoids from BAL Fluid. Am. J. Respir. Crit. Care Med. *209*, 1501–1504. https://doi.org/10.1164/rccm.202310-1831LE.

80. Lambert, G.G., Depernet, H., Gotthard, G., Schultz, D.T., Navizet, I., Lambert, T., Adams, S.R., Torreblanca-Zanca, A., Chu, M., Bindels, D.S., et al. (2020). Aequorea's secrets revealed: New fluorescent proteins with unique properties for bioimaging and biosensing. PLoS Biol. *18*, e3000936. https://doi.org/10.1371/journal.pbio.3000936.

81. Ivorra-Molla, E., Akhuli, D., McAndrew, M.B.L., Scott, W., Kumar, L., Palani, S., Mishima, M., Crow, A., and Balasubramanian, M.K. (2024). A monomeric StayGold fluorescent protein. Nat. Biotechnol. *42*, 1368–1371. https://doi.org/10.1038/s41587-023-02018-w.

82. Hufton, S.E., Risley, P., Ball, C.R., Major, D., Engelhardt, O.G., and Poole, S. (2014). The breadth of cross sub-type neutralisation activity of a single domain antibody to influenza hemagglutinin can be increased by antibody valency. PLoS One *9*, e103294. https://doi.org/10.1371/journal.pone.0103294.

83. Zeng, Q., Langereis, M.A., van Vliet, A.L.W., Huizinga, E.G., and de Groot, R.J. (2008). Structure of coronavirus hemagglutinin-esterase offers insight into corona and influenza virus evolution. Proc. Natl. Acad. Sci. USA *105*, 9065–9069. https://doi.org/10.1073/pnas.0800502105.

84. Lei, C., Yang, J., Hu, J., and Sun, X. (2021). On the Calculation of $TCID_{50}$ for Quantitation of Virus Infectivity. Virol. Sin. *36*, 141–144. https://doi.org/10.1007/s12250-020-00230-5.

85. Fouchier, R.A., Bestebroer, T.M., Herfst, S., Van Der Kemp, L., Rimmelzwaan, G.F., and Osterhaus, A.D. (2000). Detection of influenza A viruses from different species by PCR amplification of conserved sequences in the matrix gene. J. Clin. Microbiol. *38*, 4096–4101. https://doi.org/10.1128/JCM.38.11.4096-4101.2000.

86. Gaspar, I., Wippich, F., and Ephrussi, A. (2018). Terminal Deoxynucleotidyl Transferase Mediated Production of Labeled Probes for Single-molecule FISH or RNA Capture. Bio Protoc. *8*, e2750. https://doi.org/10.21769/BioProtoc.2750.

87. Lyubimova, A., Itzkovitz, S., Junker, J.P., Fan, Z.P., Wu, X., and van Oudenaarden, A. (2013). Single-molecule mRNA detection and counting in mammalian tissue. Nat. Protoc. *8*, 1743–1758. https://doi.org/10.1038/nprot.2013.109.

88. Corti, D., Voss, J., Gamblin, S.J., Codoni, G., Macagno, A., Jarrossay, D., Vachieri, S.G., Pinna, D., Minola, A., Vanzetta, F., et al. (2011). A neutralizing antibody selected from plasma cells that binds to group 1 and group 2 influenza A hemagglutinins. Science *333*, 850–856. https://doi.org/10.1126/science.1205669.

89. Schindelin, J., Arganda-Carreras, I., Frise, E., Kaynig, V., Longair, M., Pietzsch, T., Preibisch, S., Rueden, C., Saalfeld, S., Schmid, B., et al. (2012). Fiji: an open-source platform for biological-image analysis. Nat. Methods *9*, 676–682. https://doi.org/10.1038/nmeth.2019.

90. Stringer, C., Wang, T., Michaelos, M., and Pachitariu, M. (2021). Cellpose: a generalist algorithm for cellular segmentation. Nat. Methods *18*, 100–106. https://doi.org/10.1038/s41592-020-01018-x.

Please cite this article in press as: Rabouw et al., Live-cell single-vRNP imaging identifies viral gene expression signatures that shape influenza infection heterogeneity, Cell Systems (2025), https://doi.org/10.1016/j.cels.2025.101489

STAR★METHODS

KEY RESOURCES TABLE

REAGENT or RESOURCE	SOURCE	IDENTIFIER
Antibodies		
Mouse monoclonal anti-Influenza A virus NP antibody	BioXcell	Cat# BE0159; RRID: AB_10949071
Rabbit monoclonal sodium potassium ATPase antibody	Invitrogen	Ref# MA5-32184; RRID: AB_2809472
Human monoclonal anti-Influenza HA FI6 antibody	Xander de Haan lab	N/A
Alexa Fluor 647 donkey anti-mouse antibody	Invitrogen	Ref# A31571; RRID: AB_162542
Alexa Fluor 488 goat anti-rabbit antibody	Invitrogen	Ref# A11034; RRID: AB_2576217
Bacterial and virus strains		
A/Puerto Rico/8/1934	This study	N/A
A/Neth/213/2003	Fouchier lab	N/A
A/BHG/Neth/48/2018	Fouchier lab	N/A
A/Swine/Neth/3/2008	Fouchier lab	N/A
A/Swine/Gent/172/2008	Fouchier lab	N/A
A/Mal/Neth/1/2014	Fouchier lab	N/A
A/Mal/Neth/1/2005	Fouchier lab	N/A
A/Mal/Neth/143/2018	Fouchier lab	N/A
A/Mal/Neth/41/2015	Fouchier lab	N/A
A/Mal/Neth/33/2011	Fouchier lab	N/A
A/Mal/Neth/7/2018	Fouchier lab	N/A
Patient-derieved IAV (H1N1)	Fouchier lab	N/A
Chemicals, peptides, and recombinant proteins		
DMEM	GIBCO	Cat# 31966021
Leibovitz's L15 medium	GIBCO	Cat# 21083027
Opti-MEM	GIBCO	Cat# 11058021
TryplE	GIBCO	Cat# 12605010
Fetal Bovine Serum (FBS)	Sigma-Aldrich	Cat# F7524
Penicillin-Streptomycin	GIBCO	Cat# 15140122
Polyethylenimine	Polysciences Inc	Cat# 23966
Polybrene	Sigma-Aldrich	Cat# TR-1003-G
Glucose oxidase	Sigma-Aldrich	Cat# G2133-10KU
Catalase	Sigma-Aldrich	Cat# C3515-10MG
Atto488-NHS	Atto-Tec	Cat# AD 488-31
Atto565-NHS	merck	Cat# 72464-1MG-F
Atto633-NHS	Atto-Tec	Cat# AD 633-31
Alexa Fluor 647 NHS	Thermo Fisher Scientific	Cat# A20006
Dylight-488	Thermo Fisher Scientific	Cat# 11849370
Linear Acrylamide	Thermo Fisher Scientific	Cat# AM9520
Triton-X-100	merck	Cat# 9036-19-5
Amino-11-ddUTP	Lumiprobe	Cat# A5040
Ribonucleoside Vanadyl Complex	NEB	Cat# S1402S
tRNA	merck	Cat# R1753-500UN
Dextran sulfate, sodium salt	merck	Cat# D8906-50G
BSA	Thermo Fisher Scientific	Cat# 240400100

(*Continued on next page*)

Continued

REAGENT or RESOURCE	SOURCE	IDENTIFIER
Paraformaldehyde	VWR	Cat# 43368.9M
Formamide	Thermo Fisher Scientific	Cat# AM9342
Random Hexamer	Thermo Fisher Scientific	Cat# SO142
DAPI	Thermo Fisher Scientific	Cat# 62248
Hoechst 33342	Thermo Fisher Scientific	Cat# 62249
Cdk1 Inhibitor IV, RO-3306	merck	Cat# 217699-5MG
Bafilomycin A1	merck	Cat# SML1661-.1ML
Cultrex Basement Membrane Extract, PathClear	R&D systems	Cat# 3432-010-01
Human Heregulin beta-1 Recombinant Protein	PeproTech	Cat# 100-03
Invasin	Wijnakker et al.[60]	N/A
Critical commercial assays		
Tetro reverse transcriptase	Bioline	Cat# BIO-65050
Terminal deoxynucleotidyl Transferase	ThermoFisher	Cat# EP0162
Amicon Ultra Centrifugal Filter, 10 kDa MWCO	merck	Cat# UFC5010
UTM Universal Transport Medium	Copan	N/A
NucleoSpin RNA, Mini kit for RNA purification	Macherey-Nagel	Cat# 740955.50
iQ SYBR Green SuperMix	Bio-Rad	Cat# 1708885
Deposited data		
Code used in this study	Zenodo	Zenodo: http://www.doi.org/10.5281/zenodo.17606905
Raw data of imaging experiments	Mendeley data	Mendeley Data: http://www.doi.org/10.17632/6gb6rpm69w.1
Experimental models: Cell lines		
A549 cells	ATCC	Cat# CCL-185
MDCKII	Fouchier lab	N/A
HEK293T cells	Fouchier lab	N/A
Oligonucleotides		
smFISH probe sets	Table S1, ordered from IDT	N/A
qPCR primer sequences	Table S1, ordered from IDT	N/A
Recombinant DNA		
Plasmids used in this study	Tanenbaum lab	N/A
Software and algorithms		
ImageJ	NIH	https://imagej.nih.gov/ij/
NIS-Elements Imaging software	Nikon	https://www.microscope.healthcare.nikon.com/en_EU/products/software
Graphpad Prism 9	GraphPad Software Inc	https://www.graphpad.com:443/scientific-software/prism/
R 4.2.2	R Core Team[61]	https://www.R-project.org/
Rstudio 2022.12.0+353	R Core Team[61]	http://www.rstudio.com/
ggplot2 3.4.4	Wickham[62]	https://ggplot2.tidyverse.org
dplyr 1.1.4	Wickham et al.[63]	https://dplyr.tidyverse.org
MIST	Chalfoun et al.[64]	https://github.com/usnistgov/MIST
Rphenograph 0.99.1	Levine et al.[65]	https://github.com/JinmiaoChenLab/Rphenograph
umap 0.2.10.0	McInnes et al.[66]	https://cran.r-project.org/web/packages/umap/vignettes/umap.html
destiny 3.12.0	Angerer et al.[67]	https://github.com/theislab/destiny

(*Continued on next page*)

Continued

REAGENT or RESOURCE	SOURCE	IDENTIFIER
slingshot 2.6.0	Street et al.[68]	https://bioconductor.org/packages/devel/bioc/vignettes/slingshot/inst/doc/vignette.html
Python 3.9.15	Python Software Foundation	https://www.python.org/
Numpy 1.23.5	NumPy team	https://numpy.org/
Pandas 1.5.2	NumFOCUS, Inc.	https://pandas.pydata.org/
Cellpose 2.2.3	Pachitariu and Stringer[69]	https://www.cellpose.org/
Trackmate 7.9.2	Ershov et al.[70]	https://imagej.net/plugins/trackmate/
Scikit-image 0.22.0	van der Walt et al.[71]	https://github.com/scikit-image/scikit-image
Deepblink 0.1.0	Eichenberger et al.[72]	https://github.com/BBQuercus/deepBlink
BaSiCPy 1.0.1	Peng et al.[73]	https://basicpy.readthedocs.io/en/latest/
PyStackReg 0.2.7	Thévenaz et al.[74]	https://github.com/glichtner/pystackreg
Napari 0.4.17	Sofroniew et al.[75]	https://napari.org/
Big-FISH 0.6.2	Imbert et al.[76]	https://github.com/fish-quant/big-fish
Other		
96-well glass bottom imaging plates-(Matriplates)	Brooks Life Science Systems	Cat# MGB096-1-2-LG-L
384-well glass bottom imaging plates-(Matriplates)	Brooks Life Science Systems	Cat# MGB101-1-2-LG-L
μ-Plate 96 Well Square Glass Bottom	Ibidi	Cat# 89627

EXPERIMENTAL MODEL AND STUDY PARTICIPANT DETAILS

Cell lines

A549 (ATCC, Cat# CCL-185, isolated from the lung cancer of a 58-year-old white male), MDCKII and HEK293T cell lines were grown in DMEM (4.5 g/L glucose, GIBCO, Cat# 31966021) supplemented with 10% fetal bovine serum (FBS, Sigma-Aldrich, Cat# F7524) and 1% penicillin/streptomycin (GIBCO, Cat# 15140122) and regularly passaged when reaching 80-90% confluency using TryplE (GIBCO, Cat# 12605010). All cells were cultured with 5% CO2 at 37°C. Cell lines were confirmed to be mycoplasma negative.

IAV production

Generation of A/Puerto Rico/8/1934 (PR8) by a reverse genetic system was conducted as reported previously.[77] Briefly, eight plasmids encoding the individual genome segments under control of bidirectional promoters were transiently transfected into HEK293T cells using the calcium phosphate transfection method. Medium was replaced after 16 h with fresh DMEM supplemented with 2% FBS and TPCK-treated trypsin (1 μg/mL, Merck, Cat# 20233). 48 h after medium replacement, HEK293T supernatant containing virus was harvested and added to MDCKII cells for 2 h. Cells were then washed and kept in OptiMEM (Thermo Fisher Scientific, Cat# 11058021) supplemented with trypsin. MDCKII supernatant was collected after 2 to 3 days, when cytopathic effects (CPE) were observed, and stored at -80°C. Virus stocks were used for passaging on MDCKII (unless indicated otherwise) cells at low multiplicity of infection for a maximum of two passages. To produce IAV stocks in chicken eggs, eleven-day old embryonated chicken eggs were inoculated with PR8 influenza virus at low MOI. Allantoic fluid was harvested two days post-inoculation and centrifuged for ten minutes at 2,100 *g* to remove cellular debris.

Generation of PR8-HA-DIG followed the same protocol as described above with two notable differences. First, instead of a reverse-genetics plasmid encoding the full-length HA, an HA-DIG encoding plasmid was used during virus production in HEK293T cells (sequence in Table S1). To allow for virus production, a second plasmid encoding full-length HA was co-expressed, but full-length HA was expressed from a plasmid that did not generate negative-sense RNA, and as such the RNA encoding full-length HA was not incorporated in the virion as a vRNA. Second, MDCKII used for passaging of the HA-DIG virus stably express the HA protein to allow for virion production.

Clinical IAV samples

Clinical IAV samples were derived from hospitalized patients that were admitted with respiratory complaints and that tested positive for IAV. Throat or nasal swaps were collected in Universal Transport Medium (Copan) according to the according to manufacturer's protocol and stored at -80°C until further usage. The Institutional research Review Board Erasmus MC of Rotterdam, The Netherlands, confirms that the rules laid down in the Medical Research Involving Human Subjects Act (also known by its Dutch

abbreviation WMO), do not apply to this research. Anonymous left-overs of diagnostic specimens collected from individuals who did not oppose to the reuse of their specimens can be used to develop or improve diagnostic methods.

Human airway epithelial cell culture and imaging

A human airway organoid (AO) line (9209N) from an established organoid biobank was used in this study, with ethical approval granted by the NKI Institutional Review Board (IRB, M18ORG/CFMPB582).[78] AO maintenance protocols have been described previously.[28]

To generate AOs stably expressing Nb^{NP}-GFP, single-cell suspensions of passage 4 organoids were infected with a lentivirus carrying the construct encoding for Nb^{NP}-GFP, according to the protocol outlined previously.[28] After two months of expansion, organoids were dissociated into single cells and cells expressing low levels of GFP were isolated via fluorescence-activated cell sorting (FACS). The sorted cells were plated at high density (approximately 1300 cells/μL) in organoid culture conditions. To support cell survival, 50% conditioned media from healthy AO cultures and 5 nM heregulin beta-1 (PeproTech, Cat# 100-03) were added during the first week post-sorting.[79] The organoids were subsequently expanded using standard AO media.

For influenza A virus (IAV) infection studies, organoids were plated onto glass-bottom imaging plates. To promote 2D cell attachment, the plates were pre-coated either with 5% Cultrex Basement Membrane Extract, PathClear (R&D systems, Cat# 3432-010-01) in AdDMEM/F12 (incubated at 37°C for 30 minutes) or with 5 μg/mL invasin in PBS (incubated overnight at 4°C).[60] Following coating, AO cells were seeded into 96-well plates (1 million cells/well) or 384-well plates (200,000 cells/well) in AO media. Media was refreshed every 3-4 days, and cells were expanded in 2D cultures for approximately two weeks prior to IAV infection experiments.

METHOD DETAILS

Design of Nb expression constructs

The VISUN imaging technique makes use of a stably expressed NP-specific nanobody (Nb^{NP}) that was generated previously under the name Nb508.[17] The nucleotide sequence of the Nb^{NP} used in the current study is provided in the key resources table. For visualization, Nb^{NP} was fused at its C-terminus to the bright green fluorescent protein AausFP1,[80] and a nuclear localization sequence (NLS) was added to the C-terminus of the Nb^{NP}-GFP fusion protein to ensure nuclear localization. The A549 cell line expressing Nb^{NP} (A A549-Nb^{NP}–NLS cells) was used for all experiments unless stated otherwise. To quantify cytoplasmic vRNPs we generated the cell line A549-Nb^{NP}cyto, in which the Nb^{NP} was fused to the green fluorophore mStaygold without NLS.[81] To label HA protein in a live cell setting, we used a previously reported nanobody that targets HA (Nb^{HA}, previously described as Nb-B6).[82] Nb^{HA} was tagged with a C-terminal superfolderGFP or mCherry and an N-terminal CD5 secretion sequence.[83] The fusion protein was expressed stably in HEK293T cells (HEK293T-Nb^{HA}). Key plasmids used in this study are available on AddGene.

Generation of stable cell lines

Stable cell lines were generated via lentiviral transduction as described previously.[16] In brief, the pHR lentiviral plasmid encoding the transgene of interest was co-transfected along with the packaging vectors psPax and pMD2.G using Polyethylenimine (Polysciences Inc, Cat# 23966). Transfection medium was replaced with DMEM 1 day after transfection and lentivirus collected 2 days later. Lentivirus was added to recipient A549 cells (for Nb^{NP} expression) or HEK293T cells (for Nb^{HA} expression) together with Polybrene (10 mg/mL, Santa Cruz Biotechnology Inc, Cat# TR-1003-G). Spin-infection was performed for 120 min at 2000 rpm at 25°C. HEK293T cells expressing Nb^{HA} were selected by fluorescence-activated cell sorting (FACS) for highly expressing cells. To generate monoclonal A549-Nb^{NP}–NLS cells, single cells with low expression of Nb^{NP}-GFP were sorted by FACS into 96-well plates. Low expression of Nb^{NP} is crucial to allow observation of VISUN spots over the background fluorescence of Nb^{NP}-GFP. Single-cell clones were subsequently screened for low, homogenous and nuclear Nb^{NP} expression by fluorescence microscopy. An additional screening round was performed to ensure VISUN spots could be observed after infection with IAV.

To visualize IAV cytoplasmic entry (Figures 3B–3E), a high-expressing A549-Nb^{NP}–NLS clonal cell line was selected by FACS. Due to the higher level of Nb^{NP} expression, sufficient Nb^{NP} was present in the cytoplasm to allow vRNP visualization in the cytoplasm.

Nb^{HA} harvesting

HEK293T-Nb^{HA} cells were grown to 95% confluency. During cell growth, Nb^{HA} accumulated in the supernatant, which was harvested at every passage (twice a week). Supernatant was purified with a 0.22 μm syringe filter to remove cell debris and stored at 4°C until further use.

IAV growth curve analyses

To assess the impact of Nb^{NP} expression on virus fitness, IAV growth was compared between A549-WT cells and A549-Nb^{NP}–NLS cells. Cells were grown to 70-90% confluency in 24-well plates. Cells were inoculated for 2 h with IAV (MOI 0.2), washed once with PBS and further incubated in OptiMEM supplemented with trypsin (1 μg/mL). At the indicated time points, both cell supernatant and cells were harvested and frozen at –20 °C. The concentration of infectious virions in the supernatant was quantified by a $TCID_{50}$ assay. Intracellular levels of viral RNA were quantified by qPCR.

Please cite this article in press as: Rabouw et al., Live-cell single-vRNP imaging identifies viral gene expression signatures that shape influenza infection heterogeneity, Cell Systems (2025), https://doi.org/10.1016/j.cels.2025.101489

CellPress
OPEN ACCESS

$TCID_{50}$ assay

MDCKII cells were seeded in 96-wells plates. The next day, cells were washed once in PBS, after which OptiMEM supplemented with trypsin (1 μg/mL) was added. The virus stock solutions were diluted in a 10-fold serial dilution and added to the cells. After incubation for 48 h at 37°C was read out and virus titers were calculated according to the Spearman Kärber method.[84]

qPCR analysis of intracellular viral RNA

RNA was extracted from cells using the NucleoSpin RNA isolation kit (Machery-Nagel, Cat# 740955.50), according to manufacturer's protocol. cDNA was synthesized with the Tetro Reverse transcriptase (bioline, Cat# BIO-65050), according to manufacturer's protocol, using random hexamers (Thermo Fisher, Cat# SO142). qPCR was performed using IQ supermix (biorad, Cat# 1708885), with primers targeting the IAV M segment (Fw: CTTCTAACCGAGGTCGAAACG, Rv: AGGGCATTTTGGACAAAKCGTCTA).[85] As an internal control, primers targeting the host cellular GAPDH gene were used (Fw: CACCGTCAAGGCTGAGAACGGG, Rv: GGTGAAGA CGCCAGTGGACTCC). ΔΔCt values were used to calculate the fold increase of viral RNA relative to the first time point (2 h).

Drug treatments of cells

For visualization of the nucleus during live-cell imaging experiments, DNA was stained with Hoechst 33342 (Thermo Fisher Scientific, Cat# 62249) at a final concentration of 1 μg/mL. The vacuolar-type H^+-ATPases inhibitor bafilomycin A1 (BafA1, Merck, Cat# SML1661-.1ML) was used to block IAV cell entry. BafA1 was added at 50 nM final concentration after 1 h of inoculation, unless indicated otherwise. For experiments that include Nb^{HA} imaging, Leibovitz's L15 medium (GIBCO, Cat# 21083027), supplemented with 10% FBS and 1% penicillin/streptomycin, was used in a 2:1 ratio with Nb^{HA}-containing supernatant (see the 'NbHA harvesting' section) and added to the cells. To synchronize cells in the cell cycle, cells were arrested in G2 using the CDK1 inhibitor RO3306 (Merck, Cat# 217699-5MG) at a final concentration of 5 μM for 16 h (Figures 6E and 6F). To release cells from the cell cycle block, the inhibitor was removed by washing cells 3 times with L15 medium for 5 min at 37°C. Cells were directly used for imaging and only cells which underwent mitosis were included in the analysis.

Cell culture for imaging

Cells were grown in a 96-well or 384-well glass-bottom plate (μ-Plate, Ibidi, Cat# 89627, or Matriplates, Brooks, Cat# MGB096-1-2-LG-L, Cat# MGB101-1-2-LG-L) such that cells were 70-90% confluent at the start of imaging experiments. Live cells were kept in L15 medium supplemented with 10% FBS and 1% penicillin/streptomycin during imaging experiments. Live-cell imaging was performed at 37°C at atmospheric CO_2 levels. Fixed-cell imaging was performed at r.t.

Live-cell imaging of viral entry

For experiments focusing on vRNP entry dynamics (Figures 3, S1H, and S4), entry into host cells was synchronized using an assay in which the pH of the cell culture medium was used to control viral entry. Briefly, cells were cultured in DMEM and incubated at atmospheric CO_2 levels for 5 min, during which time pH level of the medium increases to ~9.5. Then, virus inoculation was performed and virions were allowed to attach to cells and undergo endocytosis for 30 min. Due to the high pH, virus fusion with the endosome is prevented at this time. To stimulate synchronous viral entry, DMEM was then exchanged with L15 medium, which has a pH of 7.0-7.4 at atmospheric CO_2 levels. The sudden change in pH allows natural endosomal acidification, leading to rapid release of the virus. Image acquisition of VISUN signal was either started at the time of the medium exchange (Figures 3 and S4A) or immediately after virus inoculation, but before the pH change (Figure S4B). For comparing nuclear import rates of vRNPs between A549-WT and A549-Nb^{NP}-NLS cells (Figure S1H), cells were fixed after the indicated incubation time periods in L15 (0-15 min).

smFISH

smFISH experiments were conducted as reported previously.[16,86,87] For all target RNAs, complementary, short DNA oligonucleotides (20 nucleotides long, at least 48 probes per RNA) were designed using Stellaris probe designer (https://www.biosearchtech.com/support/tools/design-software/stellaris-probe-designer) and ordered from Integrated DNA Technologies (IDT). All smFISH probes targeting a single RNA were pooled ('smFISH probe sets') to a concentration of 200 μM. Probe sets were subsequently labelled using fluorescent Amino-11-ddUTP (Lumiprobe, Cat# A5040), which was conjugated to Dylight-488 (Thermo Scientific, Cat# 11849370), Atto-565 or Atto-633 NHS ester (AttoTec, Cat# 72464-1MG-F and Cat# AD 633-31). Ligation of fluorescent Amino-11-ddUTP to the probes was performed using Terminal deoxynucleotidyl Transferase (TdT) (Thermo Scientific, Cat# EP0162) according to manufacturer's protocol. After labeling, probe sets were washed 3 times in 70% ethanol and resuspended in nuclease-free water.

For smFISH staining, cells were fixed in 4% paraformaldehyde (VWR, Cat# 43368.9M) in PBS for 15 min, and subsequently permeabilized in ethanol at 4°C for 30 min. Then, cells were washed twice in smFISH wash buffer (10% formamide (Thermo Scientific, Cat# AM9342), 2xSSC in nuclease-free water). Probe sets were diluted to 10 nM final concentration in hybridization buffer (10% formamide, 2xSSC, 10% dextran sulphate (Merck, Cat# D8906-50G) tRNA (1 mg/mL, Merck, Cat# R1753-500UN), Ribonucleoside Vanadyl Complex (2 mM, NEB, Cat# S1402S), BSA (200 μg/mL, Thermo Scientific, Cat# 240400100) in nuclease-free water). Diluted probe sets in hybridization buffer were added to cells, and hybridization was performed overnight at 37°C. Samples were then washed twice with smFISH wash buffer supplemented with DAPI (10 μg/mL, Merck, Cat# 62248) for 1 h at 37°C, and stored in PBS at 4°C until imaging. For iterative smFISH staining, smFISH probes were removed through incubation of samples with 80%

formamide at r.t. for 6 h. After stripping away the smFISH probes, the staining protocol was repeated for a new set of smFISH probes. The efficiency of probe removal was confirmed by imaging.

Virion smFISH

For experiments in which colocalization between vRNA and Nb^{HA} was assessed (Figure S3), virus stocks were diluted in Nb^{HA}-containing supernatant (see 'NbHA harvesting'). To attach virions to the glass for imaging, the solution containing the virus was added to 96-well glass-bottom plates and incubated for 3 h at 37°C. Subsequently, samples were fixed and stained as described in the 'smFISH' section. All viral genome segments were stained with probe sets labelled with Atto-633. Single z-planes were imaged by confocal microscopy. Spots in each channel were identified, and colocalization assessed in automated fashion using the ComDet FIJI plugin (https://github.com/UU-cellbiology/ComDet).

For experiments to determine the frequency that each genome segment was missing from virions (Figures 6B–6D), virions were diluted (1:30) in PBS and added to 96-well glass-bottom plates for 3 h at 37°C. Virions were then fixed and stained as described in the 'smFISH' section. Three genome segments were stained in each sample using probe sets labeled with Dylight-488, Atto-565, and Atto-633. Single z-planes were imaged by confocal microscopy. Spots in each channel were identified, and colocalization assessed in automated fashion using the ComDet FIJI plugin. Colocalization of at least two probe sets was used to identify the location of a virion. Colocalization of the third channel (either Atto-565 or Atto-633) was quantified, and reports on the fraction of virions in which the vRNA of interest is present. To assess probe set sensitivity, samples were taken along for all probe sets in each experiment, in which the same genome segment was labeled with probes sets labeled with both Atto-568 and Atto-633 and colocalization was scored to determine probe sensitivity. Each value shown in Figure 6 is corrected for the probe set sensitivity. Packaging efficiency of seven of the eight genome segments could be assessed via this method. smFISH probes for the (-)M segment failed to give sufficient signal for accurate analysis. Each datapoint indicates a separate experiment, which includes five to ten images containing ~100-200 virions each.

Immunofluorescence (IF) staining

Primary antibody labelling

The previously published monoclonal human FI6 antibody targeting the IAV HA protein[88] was a kind gift of Xander de Haan. To fluorescently label the FI6 antibody with the Alexa Fluor 647, the antibody (2.5 mg/ml) was transferred to 0.1M sodium bicarbonate (pH 8.3) buffer. The Alexa Fluor 647 NHS dye (Thermo Scientific, Cat# A20006) was dissolved in DMSO and added to the FI6 antibody in a 3:1 molar ratio. The reaction was incubated for 4 h at r.t. using head-over-head rotation. The primary labelled antibody was purified using a 10 kDa MWCO Amicon Ultra Centrifugal Filter (Merck, Cat# UFC5010), following the manufacture's protocol, and eluted in 100 μl PBS.

IF staining procedure

Cells were fixed in 4% PFA in PBS for 15 min, and permeabilized with 0.5% Triton-X100 (Merck, Cat# 9036-19-5) in PBS for 5 min. After fixation, block buffer was added (2% BSA, 50 nM ammonium chloride in PBS) for 30 min, followed by 45 min incubation with the primary antibody in block buffer. Samples were washed 5 times in block buffer, and subsequently incubated for 45 min with the secondary antibody and DAPI. After incubation with secondary antibodies, cells were washed once with block buffer and once with PBS. All steps were performed at r.t., and the samples were stored in PBS at 4°C until imaging. IF for NP was performed using the mouse monoclonal anti-Influenza A virus NP antibody HB-65 (10 μg/mL, BioXcell, Cat# BE0159) in combination with secondary Alexa Fluor 647 donkey anti-mouse antibody (10 μg/mL, Invitrogen, Cat# A31571). For HA labelling, Alexa Fluor 647 labeled FI6 antibody was used (1:100 dilution). For general cell membrane staining, the sodium potassium ATPase recombinant rabbit monoclonal antibody (10 μg/mL, Invitrogen, Cat# MA5-32184) was used as primary antibody, followed by the secondary Alexa Fluor 488 goat anti-rabbit antibody (10 μg/mL, Invitrogen, Cat# A11034).

Combined smFISH and IF staining

For experiments in which IF staining was combined with smFISH staining, the complete smFISH protocol was performed as described in the 'smFISH' section, followed by the complete IF protocol as described in the 'IF staining procedure' section. For the multiplexed smFISH experiments, IF staining was performed for the sodium potassium ATPase, a protein localized to the plasma membrane, to identify cell outlines that could be used for cell segmentation. Sodium potassium ATPase staining was performed in the GFP channel, which overlapped with the green fluorescence from the Nb^{HA}. However, fluorescence of the Nb^{HA} had been chemically bleached by the iterative smFISH protocol.

Microscopy

Hardware

Fluorescence microscopy of all live and fixed cell experiments was performed using a Nikon TI2 inverted microscope controlled by the NIS Elements software (Nikon), equipped with a CSU-X1 spinning disc (Yokagawa) and a Prime 95B sCMOS camera (Photometrics). For imaging, a 60x/1.40 NA or a 40x/1.30 NA oil-immersion objective was used. z-drift was corrected using the Nikon perfect focus system. The microscope stage was equipped with a temperature-controlled box to conduct live-cell experiments at 37°C and fixed-cell experiments at r.t.

Please cite this article in press as: Rabouw et al., Live-cell single-vRNP imaging identifies viral gene expression signatures that shape influenza infection heterogeneity, Cell Systems (2025), https://doi.org/10.1016/j.cels.2025.101489

Microscopy acquisition settings

In all experiments, a 50 ms exposure time was used for all laser lines. For long-term live-cell acquisitions, a large field of view (FOV) was created by computationally stitching single FOVs post acquisition (see 'image stitching' subsection). The generation of a large FOV allows robust tracking of cells over longer periods of time, even with substantial cell migration. For example, for live-cell experiments combined with multiplexed smFISH, 210 individual FOVs organized in a 15x14 x,y-grid were acquired and stitched post-acquisition. The time interval in long-term live-cell experiments running less than 24 h was set to 15 min, unless indicated otherwise. For each x,y-position, 3 z-slices (1 μm step size) were acquired. VISUN images were acquired in the GFP channel, Hoechst 33342 in the BFP channel and Nb^{HA} either in the GFP channel or the mCherry channel. Nb^{HA}-GFP was used for experiments shown in Figures 2B, 3J, 3K, 4F-4I, 5 (progression score), S1M, S3A, S3D, S3E, S6A, S7D–S7G, and S8F, and Nb^{HA}-mCherry as shown in Figures 3G, 4D, 4E, 5K, S1J, S3B–S3D, S5A, S5D, and S5E.

Short-term imaging for counting of the number of vRNP spots (Figures 4C, 6A, 6D–6F, 6H, 6I, S1D, S8C, and S9A) or analyses of vRNP entry dynamics (Figures 3A–3F) was conducted without delay between acquired images (using 50 ms exposure) using a single z-slice. To determine vRNP spot number per cell, single x,y positions were imaged for 20 s. For virus entry experiments, single FOVs were imaged simultenously with pH value adjustment for up to 10 min.

For experiments in which live-cell imaging was combined with fixed-cell imaging, fixation of cells was performed immediately after acquisition of the last time point of the live-cell experiment. After staining, either following the smFISH or IF protocol, samples were aligned to the same x,y positions acquired during the live-cell experiment. For each x,y-position, 5 to 13 z-slices with 1 μm step size (stained cells), or a single z-slice (stained virus particles) were imaged.

QUANTIFICATION AND STATISTICAL ANALYSIS

Maximum intensity projection of z-slices

Before further analysis, maximum intensity projections of all z-slices were generated by either Nikon NIS-Elements AR (5.21.03), or upon data import using Numpy (1.23.5).

Automated processing of live-cell imaging data

All live-cell image analysis was performed using Python (3.9.7).

Illumination correction

Acquisition of images with most microscopes leads to images with non-homogeneous illumination, most commonly seen by signal decreasing towards the edges of the acquired FOV. Illumination correction for live-cell image datasets was performed using images obtained from a concentrated dye solution (4 μg/mL DyLight 488-NHS Ester), and dark images. 100 images at multiple x,y positions were acquired for both light and dark exposures, which were subsequently median-projected and used to calculate a correction matrix. The correction matrix was then applied to every single FOV.

Image stitching

Following illumination correction, the individual FOVs were stitched together into a large FOV. Stitching parameters were computed using the MIST algorithm in ImageJ on the timepoint halfway through the time-lapse and these stitching parameters were then applied to all other timepoints.[64,89] To launch stitching in ImageJ from python, the PyImageJ package was used.

Segmentation

Segmentation of nuclei was performed on the Hoechst 33342 images, using CellPose (2.2.3) with the pre-trained 'nuclei' model and an average object diameter of 80.[90]

Tracking

Tracking of cells over time was performed using the generated segmentation mask objects and the simple LAP track mode of TrackMate (7.9.2), with settings: max frame gap = 5, linking max distance = 60, gap closing max distance = 100, enable track splitting = False, enable track merging = False.[70]

Automated Nb^{HA} quantification

Measurement of object intensity was performed using regionprops_table from scikit-image (0.22.0). To quantify the intensity for Nb^{HA} signal, a custom function was added to the regionprops that computes the 1 percentile of all pixels in the nuclear area. The 1 percentile value was then background subtracted based on the mean signal of uninfected cells (based on Nb^{NP}) for all timepoints. To integrate data from replicate (n=3) experiments, the baseline subtracted intensity values were scaled between the 1^{st} and 99^{th} percentile per replicate irrespective of timepoint.

Mitosis calling

To assess the interplay of viral infection, replication and host cell mitosis we developed an approach to detect mitotic events and link sister-cells in an automated manner. Detection of mitotic cells was achieved by:

1. Extracting morphological and DAPI intensity features for all cells
2. Annotating a subset of cells in interphase and mitosis. Cells were chosen randomly across the whole time-lapse
3. Training a random forest classifier on the annotated cells
4. Applying the model to the rest of the data

Please cite this article in press as: Rabouw et al., Live-cell single-vRNP imaging identifies viral gene expression signatures that shape influenza infection heterogeneity, Cell Systems (2025), https://doi.org/10.1016/j.cels.2025.101489

For the cells and timepoints in which a mitotic event was predicted by the model, we searched for tracks that were newly initiated within a certain window of space and time (e.g. newly initiated tracks within 20 pixels in x- and y and within three timepoints in time). For each mitotic event, the newly initiated tracks within this window were then extracted and used for sister-cell linking. The predicted sister-cell linkages that were used for data analysis were validated by checking the time-lapse movies manually.

Creating single-cell grids and animations

The single-object-grid tool (see code repository) was used to crop a small FOV around tracked cells in order to create stabilized timeseries with the nuclear centroid centered. The napari-animation plugin was used to generate video output from the napari viewer to create supplemental videos.

Live-cell imaging analyses

vRNP count and virions per cell count

To determine the number of vRNPs in the nucleus or cytoplasm, infected cells were imaged for a short period of time as described in the 'microscopy acquisition settings'. Fluorescent spots were counted manually. Only cells, which were located completely in the FOV were used for analysis of spot count. In A549-Nb^{NP}-NLS cells, the location of the nucleus was verified by Hoechst 33342 staining. Since the A549-Nb^{NP}cyto cell line was polyclonal, some cells showed stationary background spots in the GFP channel, which could readily be discriminated from VISUN spots based on their mobility. Such cells were excluded from further analysis.

To determine the number of infecting virions within a single cell, the number of VISUN spots was scored as indicated above. If the number ranged between 1-8, the cells were assigned to the group of one-virion infections, between 9-16 as two-virion infections, and >16 as infections with more than two virions. For most experiments, 20 s streaming acquisition was performed after 1h of inoculation to score the number of infecting virions as described in 'microscopy acquisition settings'. For experiments in which long-term imaging was started simultaneously with inoculation (Figure S2C), the number of infecting virions was determined based on the spot count in single z-slices.

Quantification of vRNP entry dynamics

For the quantification of the duration between pH adjustment and endosomal fusion, we determined the time from pH adjustment to the first observation of a (largely) immobile VISUN spot in the cytoplasm. For this analysis we included only spots that appeared after the start of imaging and that later split into smaller, mobile spots during the observation period. All other spots were excluded from the analysis, since such spots likely represent background spots. For analysis of the dynamics of endosomal release of vRNPs, only spots were included that remained in the z-plane that was imaged during the course of imaging. The first moment a spatial separation was observed between the bright immobile spot and a mobile spot was called as the moment of release of the genome segment.

Annotation of VISUN time-lapse imaging

All annotations of the life cycle stages imaged with VISUN were performed manually.

The moment of infection: The moment of infection was determined based on the first VISUN spots appearing in the nucleus. If several viral particles entered the nucleus at different time points, the moment of detecting the first spot was used.

The moment of vRNP replication: The moment of vRNP replication was determined based on the first increase in VISUN spot number after vRNP entry. The increase in number of vRNP spots had to be visible for at least three consecutive points in time of which the first one is defined as the start time of replication. In cells in which the virus replicated, single-molecule resolution was often lost after several rounds of replication, which was labeled as ''extensive'' replication (Figures 1H and S8A). Maintaining single-molecule resolution of vRNPs until the end of imaging despite vRNP replication indicates low-level vRNP replication, and was labeled as ''limited replication'' (Figure S8A). It is noteworthy that the same fluorescent spot can appear in multiple z-slices due to fast diffusion of vRNPs. Consequently, a single vRNP occasionally appears twice in images of MaxIP projection of z-slices. Therefore, an increase in spot number was determined by the trend of the average spot count per cell over time.

The moment of vRNP nuclear export: vRNP nuclear export was manually called based on a visually detectable decrease in nuclear VISUN-signal intensity and a concomitant increase in cytoplasmic VISUN-signal. We validated this approach to be quantitative and consistent by automated measurements of VISUN-intensity in the nucleus and the nuclear periphery and found that the manually called timepoint of vRNP nuclear export corresponds to the half-maximum VISUN signal intensity change between initial (pre-nuclear export) and final (post-nuclear export) situation, both in the nucleus and the cytoplasm (Figure S2E).

Annotation of Nb^{HA} signal

For determination of the moment of HA appearance at the plasma membrane, manual annotations were performed. Cells were considered positive for HA if a plasma membrane outline became detectable in the NbHA channel. The first moment a plasma membrane outline became apparent was annotated as the moment of HA appearance.

Progeny release was analyzed in experiments with low MOI (MOI < 0.05) to ensure that HA-expressing cells were spatially distant from each other (typically at least separated by one FOV). The spatial distance between HA-positive cells facilitated the identification of the cell from which progeny virions originated, which can be challenging as progeny from a single infected cell can spread out over large areas. HA-expressing cells were classified as progeny-releasing at the moment when > ~50 Nb^{HA} spots were detected in a region around the HA-positive cell that corresponds to three times the cell's own radius.

Fixed-cell experiments for vRNP nuclear export

To validate that vRNP export could be called accurately from VISUN live-cell imaging data (Figure S2D), cells were first imaged by VISUN, after which cells were fixed and stained with the NP antibody, as described under 'IF staining procedure', to examine nuclear-cytoplasmic translocation of NP (which occurs along with vRNA nuclear export). For cells in which vRNP replication occurred (as

Please cite this article in press as: Rabouw et al., Live-cell single-vRNP imaging identifies viral gene expression signatures that shape influenza infection heterogeneity, Cell Systems (2025), https://doi.org/10.1016/j.cels.2025.101489

assessed by VISUN), vRNP nuclear export was called manually based on VISUN to identify cells with or without vRNP nuclear export. The NP IF signal in nucleus and cytoplasm of both groups was analyzed in automated fashion. The cell outline segmentation was performed using an IF staining of the sodium potassium pump ATPase, which is localized to the plasma membrane. DAPI staining was used for nuclear segmentation. Segmentations were performed as described below in the section 'image analysis'. After background subtraction (using fluorescence intensity levels in uninfected cells), for each cell, the ratio between cytoplasmic and nuclear NP intensities was determined.

To examine the impact of the NLS fused to Nb^{NP} on the kinetics of vRNP nuclear export (Figure S1I), A549-WT and A549-Nb^{NP}-NLS cells were inoculated with IAV and fixed at indicated time-points post-inoculation. To assess vRNP nuclear export cells were stained using smFISH probes labeled with Atto-633 targeting all eight vRNAs. The mean cytoplasmic smFISH intensity was calculated by subtracting the total nuclear-localized signal from the total whole-cell signal. The nuclear-to-cytoplasmic ratio in fluorescence was then divided by the cytoplasmic area. Nuclei were segmented based on DAPI staining and the cell outline segmentation was performed using an IF staining of the sodium potassium pump ATPase.

Colocalization analysis of VISUN foci and viral RNA

For the colocalization analysis (Figures S1E–S1G), cells were incubated with virus inoculum and imaged for 3 h, allowing initiation of vRNP replication in a subset of cells. Cell were subsequently fixed and smFISH staining was performed, as described under 'smFISH'. (-)PB2 was stained using probes labeled with Atto-568, and (+)PB1 was stained using probes labeled with Atto-633. Images were acquired with a z-step size of 0.5 μm (see section 'microscopy acquisition settings'). To quantify colocalization of VISUN spots with (-)RNA smFISH, images were processed as follows; first, nuclei were segmented in 3D using the GFP signal from the nanobody. To enhance the performance of segmentation and remove the VISUN spots, the GFP images were first smoothed using a gaussian filter with sigma=2. The smoothed GFP images were then used for 3D nuclear segmentation with cellpose 2.0, using the parameters: *Choose_3D_mode = "3D predictions", Object_diameter = 80, Anisotropy = 3, Min_size = 20000, mask_threshold=0, model = models.Cellpose(gpu=False, model_type='nuclei')*.[90] As a second step, the VISUN and (-)RNA smFISH spots were detected using deepblink.[72] More specifically, the deepblink model 'smfish2' was applied with *probability = 0.000001*. The spot detection was performed on each z-slice separately. To ensure that the same spot is not detected multiple adjacent z-slices, a 3D refinement step was included to find the center of the spot in the z-dimension, as described previously (https://github.com/BBQuercus/deepBlink/blob/master/examples/3d_prediction.ipynb). In brief, detected spots are tracked along the z-axis and the z-slice with the highest intensity is selected as the z-coordinate of the spot. Thirdly, since fixation can affect the VISUN spots, cells with clear VISUN spots were manually selected. Finally, colocalization was assessed by quantifying whether a VISUN spot was found within a 3-pixel distance (550nm in xy, 1.5um in z) of the detected (-)RNA spot. Since colocalization can occur due to randomness rather than specific colocalization, especially if the number of spots is high or the volume in which spots are detected is small, we analyzed the amount of random colocalization to ensure that the observed values are significant. To determine the amount of random colocalization, the same segmented nuclear 3D masks as above were used and the same number of spots that was detected for each nucleus was seeded randomly within the nuclear volume. Colocalization was then calculated as described above and compared to the observed values.

Quantification of vRNP nuclear import rates

To examine the impact of the NLS of Nb^{NP}-NLS on the kinetics of vRNP nuclear import in early infection (Figure S1H), infection by WT IAV was synchronized in A549-WT and A549-Nb^{NP}-NLS cells using the pH change assay (see 'live-cell imaging of viral entry') and cells were fixed at the indicated times post-pH change. After fixation, smFISH staining was performed for (-)PB2 (Atto-633) to determine nuclear import of the PB2 vRNP. In this analysis, we ensured that all (-)PB2 smFISH foci represented vRNPs that had entered the cell, rather than vRNPs present in intact virions either attached to the outside of the cell or present in endosomes. To this end, we excluded (-)PB2 spots if they colocalized with (-)PB1, (-)PA, (-)NP and (-)HA smFISH foci, as such (-)PB2 spots likely represent intact virions. Nuclear segmentation and colocalization analyses were performed as described in 'colocalization analysis of VISUN foci and viral RNA'.

Quantification of VISUN spot count after vRNP replication

To corroborate that VISUN spot number increase, as observed in time-lapse imaging, accurately reports on vRNP replication, cells were first imaged using VISUN to call replication, after which vRNA content was assessed by smFISH (Figures S2B and S2C). Cells were inoculated with virus, and imaged for 4 h. Cells were then grouped based on the number of infecting virions (1, 2, >2), and based on whether vRNP replication was observed by VISUN, see sections 'annotation of VISUN time-lapse imaging' and 'vRNP count and virions per cell count'. For each of the resulting six groups of cells, the count of (-)RNA smFISH spots was determined.

Calculation of expected success rates

The expected success rates for vRNP replication, vRNP nuclear export, HA synthesis and progeny release for two or three virions (Figure 4G) was calculated by assuming that each virion has an independent and equal chance to successfully accomplish the respective infection cycle step. Calculations for expected success of two virion infections were performed using the equation:

$$P(A \cup B) = P(A) + P(B) - P(AB), \quad \text{(Equation 1)}$$

and calculations of the expected success rates of three virion infections using the equation:

$$P(A \cup B \cup C) = P(A) + P(B) + P(C) - P(A \cap B) - P(A \cap C) - P(B \cap C) + P(A \cap B \cap C), \quad \text{(Equation 2)}$$

where P(*A*), P(*B*), and P(*C*) are the success rates of the individual virions for the indicated infection cycle phase, i.e. the one-virion success rates (see Figure 4F). The individual data points of the calculated success rate in Figure 4G were based on the success rate values obtained in the independent experimental repeats shown in Figure 4F.

Analysis of multiplexed smFISH

The following section refers to results presented in Figures 5, 6, S6–S8, and S10.

Image analysis

Overview. Since live-cell data was generated in large FOVs (see 'microscopy acquisition settings'), the multiplexed smFISH readouts that were subsequently generated were also acquired in large FOVs, so that all single cells could be easily matched between live and fixed data. To achieve interpretable information from all rounds of the iterative smFISH readout (see 'smFISH') that can be matched with the live-cell imaging data, several key steps have to be performed, which are described in more detail below. All image analysis was performed using python 3.9.15.

Illumination correction. To correct for non-homogeneous illumination in the multiplexed smFISH experiments, we used post-acquisition illumination correction using the BaSiC algorithm.[73] Post-acquisition illumination correction allows calculation of a correction model to correct uneven illumination, given that there are enough images to measure uneven illumination. The correction model is calculated for each channel separately, since uneven illumination can be specific for optical setups of different channels. To ensure that there are sufficient images to calculate the correction, all images that were acquired across the whole experiment (from all iterations of smFISH staining) were collected, resulting in ~2,000 images per channel. The python implementation of the BaSiC illumination algorithm was used to compute a separate illumination correction model for each channel using the function and parameters *BaSiC (get_darkfield=True, smoothness_flatfield=1)*.[73] The models were applied to the respective channels and the corrected images were saved.

Image stitching. Following illumination correction, the individual FOVs were stitched together into a large FOV using the MIST algorithm in ImageJ. Stitching was performed on each staining round separately, since the stage could have shifted between iterations of smFISH. To make sure that stitching is consistent between channels of the same acquisition, the best stitching parameters were first computed on the DAPI channel (that is present in each acquisition of the iterative smFISH experiments) and these stitching parameters were then applied to all channels of the same acquisition.

Image registration of staining rounds. To allow for quantitative measurements of the same cells across all staining rounds, it is important that the large FOVs that were generated are aligned to each other. The image alignment, or registration, was performed on the DAPI channels of each staining round and then applied to all other channels of the same staining round. To perform registration of one image to another, a reference image has to be selected. In this case, the stitched DAPI image from a staining round half-way through all staining rounds was selected as the reference image. The reference DAPI image was then used to compute the best transformation for the stitched DAPI image of each acquisition, yielding a transformation that is specific for each staining round and is applied to the other channels of the respective staining round. Registration was performed using the python package pystackreg, a python implementation of the StackReg algorithm.[74] More specifically, the registration was performed using affine transformation of the stitched DAPI image (Figure S6A).

Since only regions which were covered by all staining iterations are of interest, all the stitched and registered images were cropped to the region which was overlapping between all iterations.

Nuclear and cell segmentation. After illumination correction, stitching and registration, segmentation was performed to extract quantitative measurements for all cells and nuclei across all the stainings. Segmentation of nuclei and cells was performed using cellpose 2.0.[69] To segment nuclei, DAPI staining was used. Segmentation of nuclei was performed using the model_type='nuclei' with an average object diameter of 100. For cell segmentation, the membrane staining was combined with the DAPI staining to create a two-color image and cell segmentation was performed using the model_type='cyto2' with an average object diameter of 240.

The resulting segmentation masks were then visualized together with the images using the napari viewer and segmentation errors were manually corrected. Corrected segmentation masks were saved for further processing.[75]

smFISH spot detection. To quantify the number of viral and host RNAs per cell, single smFISH spots have to be detected and counted. However, expression levels of viral genes in particular range over multiple orders of magnitude, yielding cells that are too full of RNA to distinguish single smFISH spots. To address this problem, dense regions – regions in which individual smFISH spots cannot be distinguished - were decomposed into single spots, as described previously.[76] We are likely underestimating the real number of RNAs in cells with highly progressed infections because of the maximum intensity projection that is performed before starting with image analysis.

Spot detection and decomposition of dense regions yields a table with x,y-coordinates for each spot that was detected, which are used for counting spots per cell, as described in single-cell feature extraction.

Since the multiplexed smFISH is generated by sequential rounds of staining, imaging and destaining, it is important that the spot counts are not affected by signal carried over from a previous round of staining into the new round. To validate this the cells were imaged after each round of destaining and the destaining rounds were processed as described above. For each destaining, the spot detection parameters of the following staining round were applied, to make sure that the same criteria for spot detection are applied as in the staining to which its signal could be carried over. We found that signal was removed very efficiently in destaining rounds (Figure S6B).

Please cite this article in press as: Rabouw et al., Live-cell single-vRNP imaging identifies viral gene expression signatures that shape influenza infection heterogeneity, Cell Systems (2025), https://doi.org/10.1016/j.cels.2025.101489

Single-cell feature extraction. To count the number of RNA molecules in nuclei and cells, the computed segmentation masks (as described in 'nuclear and cell segmentation') and spot coordinates (as described above in 'smFISH spot detection') are combined. The spots are counted per staining and segmentation mask, yielding a table that contains the number of detected spots per mask and staining. This procedure is performed for both nuclear and cell segmentation. To extract cytoplasmic RNA counts, the nuclear counts were subtracted from the whole-cell counts. To quantify intensity of HA^{Nb} for single cells, the regionprops function from scikit-image was used.[71]

To assess whether our experimental and analysis workflow yields consistent results across staining rounds, we included one staining (PB2 negative sense staining) in round two and five and analyzed both staining rounds as described above. When comparing single-cell spot counts between the two rounds, spot counts were very consistent, with a pearson correlation of 0.95 between the two rounds (Figure S6C).

Spillover correction. Due to the high dynamic range of viral gene expression – ranging from a few molecules to hundreds of thousands – it is crucial that spot count quantifications for cells in which none or only a few RNAs are present, are not affected by highly positive neighboring cells. Spillover from highly positive cells can occur because of issues in stitching, registration or cell segmentation, or a combination thereof. To address this challenge, we developed an approach to correct for this type of spillover using the following steps for every single cell and for every staining:

1. The cell segmentation is iteratively eroded by several pixels, therefore creating new segmentation in which the outermost pixels are removed, making the cell mask smaller.
2. For each of the (eroded) segmentations, the spot count and the area of the segmentation is extracted.
3. For the next steps, only segmentation masks with a defined minimal area are used, to make sure that small cells are not shrunk too much.
   a. If the smallest three erosions have a spot count of zero, then set spot count to zero
   b. Otherwise, calculate the corrected number of spots by performing robust linear regression on the extracted spot counts as a function of the cell area.

If a cell has a lot of spots in the outer layers of its segmentation, the first counts are high but then values drop off abruptly of the mask is eroded. The robust linear regression disregards these values because they are considered as outliers, therefore correcting the value to zero or lowly positive, depending on whether the counts are zero after the drop off – indicative of a negative cell - or if a linear scaling is observed – indicative of a lowly positive cell that was affected by spillover (Figure S6D). For cells that are not affected by spillover, the spot count should scale linearly with cell size and the count is therefore largely unaffected by the correction (Figures S6D and S6E).

Linking fixed cells to live cell data. To link cells between the live-cell imaging and the multiplexed smFISH experiments, nuclear segmentation masks of both the final timepoint of live-cell imaging and the multiplexed smFISH were used. Both segmentation masks were binarized. The binarized nuclear segmentation from the fixed data was then registered to the binarized nuclear segmentation of the live-cell data using registration as described above in 'image registration of staining rounds'. The computed transformation was then applied to the non-binarized nuclear segmentations from the fixed data. Finally, for each nucleus in the live-cell data the most abundant pixel value (mode) of the transformed fixed nuclear segmentations was extracted, yielding a table with matched live-cell nuclear segmentation labels and fixed-cell nuclear segmentation labels which was saved for further processing.

Calculating RNA count cut-off values. Due to noise arising from the smFISH protocol or the subsequent analysis thereof, it is important that in particular for viral RNAs no false positive cells are introduced, which would distort the analysis of infected cells. To ensure that technical noise is not affecting our smFISH readouts, we therefore took advantage of the matched VISUN information to annotate around two hundred uninfected cells based on the live-cell imaging. The uninfected cells were used to calculate the 95^{th}-percentiles for spot counts in each viral smFISH staining, to make sure that we have a very low false discovery rate of viral RNAs. The 95^{th}-percentiles were then used to define a lower threshold for each viral staining, below which all values were set to zero (Figure S6G).

Data analysis

All data analysis was performed using R version 4.2.2 and Rstudio version 2022.12.0+353.[61] All plotting was performed using ggplot2 version 3.4.4.[62] General data wrangling was performed using dplyr version 1.1.4.[63] All boxplots shown in this study show the interquartile range with whiskers indicating the 95% confidence intervals.

Phenograph clustering. Phenograph clustering was performed on the eight measured viral (+)mRNAs.[65] To determine the best k-parameter for phenograph clustering, a range of k-parameters was selected and for each, phenograph clustering was performed on the dataset. Silhouette score was then used as a measure of clustering quality, as defined by the similarity within vs between clusters. In addition to silhouette score, the resulting cluster size was taken into account and k=40 was determined as the best parameter (Figure S7A).

UMAP. UMAP projections were computed using the umap function from the umap package version 0.2.10.0.[66] The umap function was run on the eight measured viral (+)mRNAs, with default umap parameters, except min_dist=0.9.

Viral progression score. To compute the viral progression score (Figures S7D and S7E) the following features were used:

- total viral (+)RNA in the nucleus and cytoplasm, calculated by summing up the eight viral (+)RNAs that were measured

- total viral (-)RNA in the nucleus and cytoplasm, calculated by summing up the three viral (-)RNAs that were measured: PB2, PB1 and NP
- mean HA protein intensity of the eroded cell segmentation. Cell segmentations were eroded by 30 pixels to reduce spillover from highly HA positive cells into neighboring cells.

All features were first log-transformed using y = log10(x+1) and the log-transformed features were scaled using the scale function of the base R package.

To compute the progression of infection score, cells were first reduced into 2D space using the DiffusionMap function of the destiny package with default settings except k=800 (Figure S7D).[67] Analysis of the diffusion maps showed a group of cells that was distinct from the rest of cells. Upon closer inspection these cells turned out to be only (-)RNA positive because they were neighboring highly infected cells that were likely budding new virus that attached to neighboring cells. Since these cells are not reflecting an ongoing infection but rather proximity to a highly infected cells, we removed them from downstream analysis. Using k-means with default parameters except centers=4 and n_start=50 allowed for easy detection and removal. Upon removal of the false positive (-)RNA cells, the diffusion map was computed again on the remaining cells using the same parameters as mentioned above. To align cells along a continuous trajectory through the diffusion map, the R package of the slingshot algorithm was used (Figure S7D).[68] The positions for single cells along the trajectory through the diffusion map were then extracted using the getCurves and slingPseudotime functions. For all subsequent analyses, the viral progression score refers to this computed trajectory, which is also shown in Figure S7D (blue arrow).

Statistical testing. Unless indicated otherwise, for statistical testing a two-sided t-test was performed. For paired data (Figures 6A and 6I), a paired, two-sided t-test was performed. In Figures 5H and 5J, statistical significance was determined through a one-way ANOVA with Dunnett post-hoc test. P-values are indicated as n.s., *, **, *** for non-significant, p-value < 0.05, p-value < 0.01 and p-value < 0.001, respectively.